**Along and across-axis variations in crustal thickness and structure at the Mid-Atlantic Ridge at 5° South obtained from wide-angle seismic tomography: Implications for ridge-segmentation**

Lars Planert [1,*], Ernst R. Flueh [1], and Timothy J. Reston [2]

(1) IFM-GEOMAR, Leibniz Institute of Marine Sciences at the University of Kiel, Wischhofstr. 1-3, D-24148 Kiel, Germany.

(2) School of Geography, Earth and Environmental Sciences, University of Birmingham, B15 2TT, United Kingdom.

(*) corresponding author: Lars Planert, IFM-GEOMAR, Leibniz Institute of Marine Sciences at the University of Kiel, Wischhofstr. 1-3, D-24148, Germany, phone: +49-431-600-2337, fax: +49-431-600-2922, e-mail: lplanert@ifm-geomar.de

accepted for publication in *Journal of Geophysical Research (JGR).*

## Abstract

Two end-member styles of crustal accretion are observed at two adjacent spreading segments at the Mid-Atlantic Ridge at 5°S: focused accretion to the segment center with rapid crustal thinning towards the transform in the northern segment and crustal thickening towards the transform at an oceanic core complex in the southern segment. Our results were obtained by tomographic inversion of wide-angle seismic reflection and refraction data collected along three intersecting profiles. The segment north of the 5°S fracture zone is characterized by a well developed median valley with a pronounced seafloor bulge in the segment center. A discrete portion of anomalously low velocities (-0.4 to -0.5 km/s relative to average off-axis structure) at depths of ~2.5 km beneath this bulge are possibly related to the presence of elevated temperatures and perhaps small portions of partial melt. This suggests that this segment is currently in a magmatically active period, which is confirmed by the observation of fresh lava flows and ongoing high-temperature hydrothermal activity at the seafloor. Close to the current spreading axis, the crust thins rapidly from 8.5 km beneath the segment center to less than 3 km beneath the transform fault which indicates that melt supply here is strongly focused to the segment center. The

reduction in crustal thickness is almost exclusively accommodated by the thinning of velocity portions indicative of seismic layer 3. The transform fault is characterized by more uniform velocity gradients throughout the entire crustal section and very low upper mantle velocities of 7.2-7.3 km/s indicating that serpentinization could be as much as 25% at 3.5 km depth. In contrast, ~4.1 Ma old crust of the northern segment shows only minor thinning from the segment center towards the segment end. Here, the transform is characterized by a normal seismic layer 2/3 transition suggesting robust melt supply to the segment end at those time. In the adjacent southern segment, the crust thickens from ~2.5 km beneath the flank of an oceanic core complex to ~5.0 km at the segment boundary. The observed changes in crustal thickness show a significant temporal and lateral variability in melt supply and suggest a more complex crustal emplacement process than predicted by models of focused melt supply to the segment centers.

## 1. Introduction

Crustal accretion at slow spreading mid-ocean ridges is thought to reflect the three-dimensional geometry of mantle and magma-flow beneath the ridge [*Kuo and Forsyth*, 1988; *Lin et al.*, 1990; *Lin and Phipps Morgan*, 1992]. Although mantle upwelling and thus magma-supply can be two-dimensional, sheet-like flow, melt migration at shallower depths is focused towards segment centers [*Magde and Sparks*, 1997]; the diversion of magma from the segment ends means that spreading there is primarily accommodated by tectonic rather than magmatic extension. As a consequence, large variations in the structure of the oceanic crust are predicted [*Tolstoy et al*., 1993; *Cannat*, 1995; *Detrick et al.*, 1995; *Karson*, 1998].

Seismic studies have revealed a disproportional thinning of the higher density lower crust at the segment boundaries, which suggests that the along-axis crustal structure is not uniform [*Tolstoy et al., 1993*; *Hooft et al.*, 2000; *Canales et al.*, 2000a]. This implies that the thinner crust at ridge-offsets is consistently less dense and, in contrast, the thicker crust at segment centers is consistently denser than average. Together, this results in an underestimation of the crustal thickness variations interpreted from gravity data [e.g., *Kuo and Forsyth*, 1988] and reveals clearly that seismic data are needed to better constrain the crustal thickness variations and possible changes in the crustal velocity structure. This is in particular due for the vicinity of ridge-transform intersections, where these variations are typically more pronounced.

Another type of geological settings known for their significant variations in crustal lithology are oceanic core complexes (OCCs) [e.g. *Tucholke and Lin*, 1994]. OCCs are domal bathymetric highs interpreted as exposed footwalls of detachment faults which are responsible for the exhumation of lower crustal and upper mantle rocks to the seafloor [*Cann et al.,* 1997; *Escartin & Cannat* 1999; *Tucholke et al.,* 2001; *Reston et al.,* 2002; *MacLeod et al.,* 2002; *Escartin et al.,* 2003]. Positive residual mantle Bouguer anomalies [e.g. *Blackman et al.,* 1998] as well as high seismic P-wave velocities and velocity gradients directly beneath the seafloor [e.g. *Canales et al.,* 2008] demonstrate that the formation of these features results in the emplacement of significant portions of high-density/ high-velocity material at shallow depths. Deep drilling into three OCCs, two at the Mid-Atlantic Ridge and one at the Southwest Indian Ridge, has recovered in each case a thick gabbro unit [*Dick et al.,* 2000, *Blackman et al.,* 2006, *Kelemen et al.,* 2004]. However, the deeper geometry and thickness of these units are still unknown and it is not clear whether they are a common feature of these structures. Recent studies conducted at Kane, Dante, and Atlantis OCC show that the position of local plutonic complexes along the ridge axis

varies in space and time suggesting that in this particular setting melt extraction from the mantle is not necessarily focused at the segment center but occurs as a more heterogeneous process [*Dick et al.*, 2008; *Canales et al.*, 2008].

The Mid-Atlantic Ridge (MAR) exhibits a wide variety of hydrothermal systems, and it is assumed that the diversity of hydrothermal styles is linked to the tectonic and magmatic processes occurring at or near the ridge axis [e.g., *Canales et al.,* 2000b; *Singh et al.,* 2006; *Canales et al.,* 2007; *deMartin et al.*, 2007]. Seismic studies conducted near high-temperature hydrothermal settings have observed reflections from crustal melt lenses [*Singh et al.,* 2006] or tomographic images of anomalously low seismic velocities indicative of crustal partial melt [*Canales et al.,* 2000b] which suggest a direct link between high-temperature vents and crustal melt reservoirs. This hypotheses can be investigated in the segment north of the 5°S fracture zone, where three high-temperature hydrothermal fields are situated on top of a pronounced seafloor bulge in the segment center [*Haase et al*., 2007; *German et al.*, 2008].

In this paper we apply a tomographic inversion of good quality seismic data to demonstrate the dramatic variations in crustal structure at a spreading segment at 5°S due to the effect of focused melt supply and magmatism. Moreover, we provide a detailed view of the type of geologic setting that can host high-temperature hydrothermal activity at the slow-spreading southern Mid-Atlantic Ridge. For the segment south of the 5°S fracture zone, we show that OCC formation can modify the prevailing pattern of melt extraction to such an extent that two end-member styles of crustal accretion emerge on these two adjacent spreading segments.

## 2. Geological setting

In 2000, two adjacent spreading segments near 5°S at the Mid-Atlantic Ridge were

investigated during the cruise M47/2 of the R/V METEOR (GERSHWIN experiment, Fig. 1). During this experiment a rifted oceanic core complex with a corrugated surface was discovered directly south of the 70 km ridge-transform offset. *Reston et al.* [2002] demonstrated that this core complex was formed at the inside corner of a fossil spreading axis and was later split by a change in the location of active seafloor spreading, resulting in an outside corner massif and the absence of an axial volcanic ridge in the northernmost part of the median valley. Thin crust in the median valley and active normal faulting reveal evidence for ongoing tectonic extension and indicate that the processes which led to the rifting of the oceanic core complex may still continue today [*Reston et al.*, 2002; *Tilman et al.*, 2004].

In contrast, the segment north of the 5°S FZ shows a very different morphology. The depth of the median valley seafloor shallows from more than 4 km close to the transform to around 3 km near the central part of the segment, close to 4°48'S, where it forms a broad 10 km wide plateau (Fig. 1). Three hydrothermal fields are situated within a 2 km long region on top of this bulge [*Haase et al., 2007*; *German et al.,* 2008]. Fluid temperatures of 407°C (the highest vent temperatures measured so far at the MAR) indicate that the fluids rise without significant interaction with seawater or conductive cooling from their heat source, likely located in the shallow crust [*Haase et al.*, 2007]. Furthermore, the abundance of fresh glassy sheet flows indicates that the area is volcanically active; the seismic activity here on 25/26th of June 2002 (Advanced National Seismic System catalog; http://earthquake.usgs.gov/research/monitoring/anss/) may have been related to the emplacement of these lava flows.

North of the bulge, seafloor depths increase to maximum values of 3.8 km for the resolved portions of the median valley. Compared to the adjacent eastern bounding walls, the western scarps of the median valley are much more subdued, creating only

0.5 km rather than almost 2 km of relief. The resulting asymmetry in cross-sectional relief varies but is significant throughout the entire segment. Close to 4°32'S, the ridge-axis seems to be offset by a sinistral 2nd order ridge axis discontinuity, which would imply an along-axis segment length of ~65 km.

Off-axis, the segment is characterized by a quite regular ridge-parallel tectonic fabric. The major faults of the rift flank mountains, i.e. the former median valley bounding faults can, in some instances, be traced southward up to the 5°S FZ. In particular, there is no indication of an inside corner high on the imaged portions of the seafloor. Along the flow-line both east and west of the current segment center, a series of large seamounts can be identified, typically rising more than 0.5 km above the surrounding seafloor (Fig. 1). Their shapes vary; some of them are cut by faults and form half-moon like structures, others are almost circular with a crater-like depression on top. We speculate that the current bulge in the segment center will be subsequently sheared and rifted apart as spreading continues and thus will look like one of the dismembered seamounts off-axis; the circular seamount at 11°55'W may have formed off-axis.

## 3. Seismic data

As part of the GERSHWIN experiment, a total of seven seismic refraction profiles were acquired, of which three lines, profiles 09, 10, and 11 (Fig. 1), are discussed in this study. Profiles 09 and 10 run in along-axis direction and extend across the active transform well into the adjacent segment. Profile 10 is 110 km long and mainly covers parts of the eastern rift flank mountains with an age of ~0.8 Ma. At its southern tip, it penetrates into ~4.9 Ma crust of the southern segment (age constraints are based on the assumption of symmetric spreading of 16 mm/a half spreading rate for both

segments [*DeMets et al.*, 1990] and the location and timing of the ridge jump in the southern segment after Reston et al. [2002]). Profile 09 covers roughly 75 km of both the northern and the southern segment. The crust of its northern part is ~4.1 Ma old. Its ~1.5 Ma old southern part is mainly occupied by the inside corner high core complex (ICH). Profile 11 crosses the median valley of the northern segment directly at its shallowest portion and runs in the spreading-direction following the aligned seamount chain. With a total length of 132 km, it covers seafloor up to an age of ~3.0 Ma to the west and ~5.3 Ma to the east.

Either 12 or 13 IFM-GEOMAR ocean bottom units [*Flueh and Bialas*, 1996; *Flueh et al.*, 2002] were deployed on each profile with ~5.5 km instrument spacing. The seismic source used was a cluster of three 32 l Bolt air guns fired at constant time intervals, resulting in a nominal shot spacing of 120 m. Data processing included the localisation of the ocean bottom instruments using the arrival time of the P-wave and the exact shot point geometry. In a second step, a time-gated deconvolution was applied to remove predictable bubble reverberations to produce a signal free of the disturbing interference of multiple and primary phases [*Wiener*, 1949]. Finally, time and offset-variant Ormsby filtering was applied in which the passband moves towards lower frequencies as record time and offset increases to reduce high-frequency noise as much as possible.

In marine data variations in the thickness and velocity of the water layer cause fluctuations in the arrival times of reflected and refracted phases. Removing these fluctuations often leads to an easier identification and separation of first breaks from secondary arrivals like PmP reflections. Therefore, the shots were redatumed from sea level to seafloor (Fig. 2). The wave-field extrapolation procedure used is a Kirchhoff summation method following the approach of *Berryhill* [1979] with the asymptotic far-field approximation of *Shtivelman and Canning* [1988]. The subsequent arrival

picking was done manually on the un-corrected seismic phases guided by the corrected record sections (additional examples of seismic record sections can be found in Figs. A4-A7 in the auxiliary material).

## 4. Tomographic inversion

We chose the tomographic method of *Korenaga* [2000], which allows to determine the 2-D velocity structure together with a floating reflector from the simultaneous inversion of refracted and reflected phases. The method employs a hybrid ray tracing scheme combining the graph method with further refinements utilizing ray bending with the conjugate gradients method, and it employs smoothing and damping constraints to regularize an iterative inversion. For the three profiles, a horizontal node spacing of 250 m in the area of station coverage and 500 m at the edges of the models is employed. Vertical node spacing linearly increases from 100 m at the seafloor to 280 m at the model bottom (i.e. 12 km below seafloor). The model areas around a grid cell which are affected by a velocity update of this grid cell are controled by the correlation length [Korenaga, 2000]. We use a horizontal correlation length, which linearly increases from 1 km at the seafloor to 5 km at the model bottom, and a vertical correlation length with corresponding values of 0.1 km and 1.0 km, respectively. For reflector nodes, the appropriate smoothing length scales are taken from the horizontal 2D velocity correlation lengths at the corresponding depths. A large number of smoothing weights for each profile is tested using a single-step inversion. The optimal weight, which minimizes the roughness of the tomographic output and at the same time decreases significantly the data variance, is then held fixed during all iterations (Fig. 3). Additionally, sweeps on damping weights are done at each iteration to restrict the average perturbation of velocity nodes to maximal 2%

and the average perturbation of reflector nodes to maximal 6%. To prevent outliers from dominating the data, synthetic traveltimes with a normalized $chi^2 > 4$ are consequently excluded from each iteration.

### 4.1 Uncertainty and Resolution Tests

To evaluate the impact of different starting models and realistic data errors on the inversion, a nonlinear Monte Carlo uncertainty analysis is performed by inverting data with random errors with a large number of random initial models built by 1-D velocity profiles hung from the seafloor [e.g., *Korenaga et al.*, 2000]. The starting models have a flat Moho but variable crustal thickness due to topography and there is no velocity discontinuity at the Moho interface due to the floating reflector constraint. The 100 random initial models have average standard deviation of ~5% for initial velocities and ~10% for initial reflector depths (b.s.l.) within the model region which is controlled by available ray coverage (see Fig. A1 in the auxiliary material for additional information on the starting model randomization). Two types of random errors are applied to the observed travel times similar to *Zhang and Toksöz* [1998]: (1) common-receiver errors, a random shift of max. ±30 ms at all the shots to the same receiver, and (2) a correlated phase depending error which is caused by the traveltime picking uncertainty. The maximum amplitude of this error depends on the assigned pick uncertainty and can reach up to ±50 ms for individual traces (see Fig. A2 in the auxiliary material for additional information on data randomization). Pick uncertainties are assigned visually and range from 30 ms to 100 ms. As a counterpart to the model ensemble, 100 data sets are built by adding the two types of random errors to the picked traveltime data. On average 7-13 iterations (depending on the profile) are applied for each of the 100 Monte Carlo inversions to reduce normalized

$chi^2$ to <1. The final velocity model and Moho is then derived from averaging all Monte Carlo solutions (Fig. 4 top).

Using the 100 Monte Carlo realizations (for individual examples, see Fig. A3 in the auxiliary material), the posterior model covariance matrix is calculated [e.g., *Zhang and Toksöz*, 1998]. The square roots of the diagonal elements of the matrix are the standard deviations of the model parameters, including both velocity and reflector nodes and representing a kind of "error bar" for the average solution (Fig. 4 center). The off-diagonal elements contain some information on how independent each model parameter is resolved. An effective measure for this is the point correlation for individual model parameters [e.g., *Zhang and Toksöz*, 1998; *Hobro et al.*, 2003], which is valid for small perturbations around the average model structure, and can take values between −1 and +1. A large positive value indicates a high correlation and a large negative value a high anti-correlation, hence both cases mean that the model parameter is not independently constrained. The correlation size and shape strongly depends on the location of the individual model parameter within the model space. The size can be almost as small as the corresponding correlation lengths applied in the regularization constraints (Fig. 5). Outside the region of available stations coverage, model parameters are not independently resolved. The increased influence of the regularization constraints leads to a greater impact of the starting model, which results in a significant correlation over a wide model range (Fig. 5 bottom).

In order to demonstrate the resolving power of the data in different parts of the model, a set of synthetic tests is performed where a known model has to be resolved using the same profile geometry and data coverage as in the real experiment (Fig. 6). A set of Gaussian velocity anomalies with different amplitudes, shapes and polarities is imposed on the (smoothed) Monte Carlo derived model solution and synthetic traveltimes are computed. Gauss-noise with a standard deviation equal to the half of

the individual pick-uncertainty is added to the synthetic traveltimes, and the inversion is initialized using the minimum 1D velocity model with the flat Moho as a starting model ("ensemble mean" in Fig. A1). The ultimate aim of this approach is to test the algorithm's capability of resolving small perturbations within the original tomographic output and whether during this process structure gets mapped into different areas. From the applied synthetic tests, crustal thickness is probably constrained to better than 200 m for the central part of the model (Fig. 6d). It is also shown that the horizontal and vertical resolution is good enough to regain even small changes from the original velocity perturbation near the seafloor. At greater depth within the central part of the model velocity perturbations are still constrained. There is no evidence for excessive leakage of velocity into reflector structure or the reverse, in fact this is even true for perturbations beyond the instrument locations.

There are, however, some principal difficulties when comparing uncertainties from Monte Carlo simulations and results from synthetic resolution tests with nature, mainly because inversion methods are based upon simplified regularization (smoothness) assumptions. Moreover, our velocity models do not include a velocity discontinuity at the Moho interface. As a consequence, lower crustal and upper mantle velocities are somewhat more suspect when constrained primarily by Pn arrivals. Besides, model uncertainty will not solely depend on the starting model and data errors, but in fact also on factors like regularization constraints, the number and distribution of available data, the model parameterization, the velocity-depth ambiguity and last but not least on the size and amplitude of the velocity anomaly itself [e.g. *Bickel*, 1990; *Zelt*, 1999]. However, the applied approach provides a useful estimate of the quality of the inversion given the smoothing applied, but not absolute bounds on the possible differences between the recovered model and the underlying structure.

## 5. Results

### 5.1 Profile 09

The most prominent result for Profile 09 (Fig. 4) is the pronounced Moho-bulge beneath the southern termination of the core complex, where the thickness of the oceanic crust is reduced to ~2.5 km. Here, seismic velocities increase almost linearly from 3.5 km/s at the seafloor to >7.0 km/s at the Moho (Fig. 7 right). Upper mantle velocities can be resolved from available Pn rays and reach up to 7.8 km/s. The crust thickens away from the bulge to ~4.5 km at the southern model edge and ~5 km at the transform facing flank of the core complex. Here, velocities >6 km/s are observed within the uppermost kilometer, followed by a sharp decrease in the velocity gradient and a more gradual increase in the lower parts of the crust.

In the northern segment, velocities show a clear layer 2/3 transition: they increase rapidly from 3.5 km/s close to the sea floor to 6.5 km/s at ~1.5 km depth, followed by a more gentle rise up to 7.1 km/s at the Moho (Fig. 7 left). There is only a slight decrease in crustal thickness towards the transform (from ~6 km at 35 km profile distance to ~5.5 km at 65 km) and velocity depth profiles at the segment center are quite similar to those obtained at the segment end (Fig. 12a).

There are no reflection data available from directly beneath the transform. However, from the velocity structure it seems clear that there is not much crustal thinning and that there is a substantial layer 3 (Fig. 12a). The velocity depth profiles of the northern segment crust are typical of young Atlantic oceanic crust, though resolved Moho depths are somewhat smaller than those obtained by *White et al.* [1992].

Most of the model areas beneath the instrument locations show standard deviations

<0.1 km/s for velocities and <0.24 km for Moho depths (Fig. 4 center). Interestingly, a very low standard deviation (<0.05 km/s) is shown even for some deeper areas, for instance in the lower crustal portions beneath the transform and the ICH slope, where available ray coverage is actually quite sparse. In this particular case, this occurs because nonlinear tomography would not allow the velocities in the lower crust to be higher, otherwise sub-Moho rays would move up and reduce the velocities [e.g. *Zelt,* 1999]. Rays which finally pass through the mid-crust would travel deeper and thus constrain the lower crust if it had lower velocities. As a consequence, even with only few ray bottoming points in the final model, there is velocity constraint during previous iterations. In the upper crust and directly beneath the instruments the ray coverage is very high, but derived standard deviations for velocities rarely drop below 0.05 km/s. A comparison with results from a similar approach, where 100 random models are inverted without adding random noise to the original traveltime data, reveals that this is mainly because the introduced common-receiver errors prevent even smaller uncertainties here.

The areas beyond the seismic stations are only poorly constrained. Here, the influence of the phase depending error is greatest, because these areas are mainly sampled through deep-turning rays with an assigned large pick uncertainty. Moreover, the predominantly sub-parallel ray paths result in a greater blurring of velocity structure. But the main reason for the uncertainties is probably the sparse ray coverage (Fig. 4 bottom) resulting in smaller model updates and thus to a final model which is almost entirely governed by the applied smoothness regularizations.

### 5.2 Profile 10

On Profile 10 the crust forms a ~8.5 km thick root near the center of the segment and

systematically thins along-axis to ~6 km in 20-23 km distance from the center before reaching its minimum of ~2.8 km close to the transform (Fig. 8). Farther south, crustal thickness increases again to values >4.5 km. Crustal velocities in the northern segment reveal a clear layer 2/3 transition as well as a significant portion of velocities 6.5-7.2 km/s and velocity gradients of ~0.15 $s^{-1}$, which are indicative of seismic layer 3. Since the thickness of the upper high-gradient portion of the crust remains relatively constant, most of the observed crustal thickness variations are accommodated by the lower crust (Fig. 12b).

The northern segment is characterized by seafloor velocities of 2.6-3.2 km/s, where the lower values are consistently found away from the segment center. Model areas closer to the transform are characterized by increasingly lower velocities, especially in the upper portion of the crust, and there is a distinct change in gradient associated with the 5.5 km/s velocity iso-line (Fig. 12b). Lower crustal velocities do not reach up to 7 km/s throughout the resolvable depth range. In contrast, model areas directly beneath the transform reveal higher seafloor velocities, and corresponding velocity profiles are characterized by more uniform velocity gradients throughout the entire crustal section, resulting in very low upper mantle velocities of 7.2-7.3 km/s at ~3.5 km depth below seafloor (Fig. 12b).

Calculated standard deviations for velocity nodes are mostly <0.1 km/s and in cases drop below 0.05 km/s (Fig. 8 center). The standard deviation of the crust-mantle interface is highest (~0.4 km) between 70 km and 85 km, associated with a local gap in reflection coverage, but usually takes lower values than 0.25 km for both the thinner and thicker portions of the crust.

Near the transform fault, mantle turning rays penetrate through the uppermost 1-1.5 km beneath the Moho (Fig. 8 bottom). A closer examination of sub-Moho velocities in all Monte Carlo solutions reveals a cluster around average values of 7.2-7.3 km/s

(Fig. 8 inset). Calculated point correlations in this particular region confirm that the reflector depth is indeed independently resolved. Although placed relatively close to the model edge, there is no evidence for a remaining influence of the starting models, which would e.g. become apparent in a significant correlation with reflector nodes at the very model edges (Fig. 9 top). In fact, this is also true for a velocity node placed at 0.8 km depth beneath the Moho. However, in case of the latter, there is evidence for a stronger correlation with neighboring velocity nodes even across the reflector (Fig. 9 bottom). For the previous evaluation of sub-Moho velocities, this suggests that obtained results may still suffer from conciderable lateral averaging with lower crustal velocities and hence may fail to predict correctly the maximum extent of the observed velocity perturbation.

### 5.3 Profile 11

Profile 11, which runs in flow-line of the segment center, reveals a portion of anomalously low velocities centered on the spreading axis (Fig. 10). Compared to the off-axis crust beneath the rifted flanks, the velocity contrast can exceed 0.7 km/s in depths of 2-2.5 km b. sf. where most of the crustal rays turn. However, the vertical extent of this negative anomaly reaches throughout the whole sampled depth range (Vp=6.5 km/s are not reached until 4.2 km below the seafloor). A region near kilometer 40, where velocities >6.5 km/s are placed at mid-crustal levels, suggests that the anomalously low velocities in these depths are restricted to a 10-15 km wide band centered on the spreading axis.

Off-axis, the lower crust is characterized by velocities of 6.5-7.2 km/s, indicative of a normal seismic layer 3 (Fig. 12c). At 9.2 km, the crust is thickest slightly east of the spreading axis and thins out to 6.6 km at the eastern model edge. Uppermost mantle

velocities are constrained for a relatively small model portion at ~95 km profile distance. Testing different upper mantle velocities in the forward computational step, the smallest RMS is obtained assuming upper mantle velocities of 7.7-7.8 km/s (Fig. 10 inset).

A synthetic resolution test is performed to assess the method's ability to recover the anomalous velocities beneath the median valley (Fig. 11). A starting model is obtained by horizontally averaging the Monte Carlo derived velocities in the area of available stations coverage (20-100 km), but excluding the region of anomalous velocity structure beneath the median valley (40-60 km). This model contains the 1-D "background" (i.e. without the low-velocity anomaly) structure of the well resolved velocity portions of Profile 11. A synthetic anomaly similar to the observed one is superimposed on the background velocities. Traveltimes are obtained from this model and from the Monte Carlo derived Moho, and are supplemented with Gaussian noise (standard deviation equal to the pick uncertainty). Inversion is started from the background model and a flat Moho to invert for the known model structure.

Within the shallowmost 1.5 km below seafloor, recovery is best revealing very similar perturbational shapes and amplitudes. In depths of the highest original perturbation (2-3 km b. sf.), between 65% and 70% of the maximum amplitudes are regained (Fig. 11b). At greater depths, the recovered velocity structure shows enhanced blurring, but observed amplitudes reach up to 80% of the original values. Recapitulating the fact that the first ~25 km of the Moho are not sampled by reflections and therefore entirely governed by the smoothing constraints, there is no major leakage of velocity into reflector structure discernable in the resolvable model portions. Hence, from the synthetic inversion with a test anomaly confined to the median valley, it is shown that the model resolution is good enough to account for the observed low velocities. Fig. 11c shows the point correlation for a velocity node placed at 2 km depth beneath the

median valley seafloor. Results indicate that velocity nodes placed at these depths indeed do not suffer from greater lateral leakage. However, the predicted uncertainty (Fig. 10 center) underestimates the actual mismatch between the observed and recovered anomaly in this area, which indicates the limitations of the Monte Carlo uncertainty analysis in the way it is applied in this study (cf. section 4.1).

## 6. Discussion

### 6.1 Evidence for elevated temperatures in the axial mid-crust

The observed low velocity zone (LVZ) beneath the median valley is clearly anomalous. The velocity depth profile in Fig. 11b shows a deviation of -0.4 km/s at a depth of 2.5 km below seafloor compared to "background velocities" (i.e. the average velocity model without the low velocity anomaly in the median valley) of Profile 11. Velocity depth profiles on the spreading axis reveal a clear change in the velocity gradient close to 1.5 km depth below seafloor, most likely related to the layer 2/3 boundary (Fig. 12c). This suggests that the observed minimum in the LVZ at 2.5 km depth is placed well into the mid crust. Since the seismic structure off-axis at similar levels is that of a relatively normal layer 3, it seems unlikely that petrological differences account for the observed anomalies. Possible causes include a gabbroic lower crust with reduced velocities due to cracks, elevated temperatures and/or small portions of partial melt.

The abundance of cracks and pores in the gabbro section is significantly reduced compared to the overlying highly fractured basaltic material because lithostatic pressure and ductile flow are likely to close pores and small cracks at greater depths. Although hydrothermal veins are not uncommon in the gabbro section [e.g., *Karson*

1998], the very consistent seismic velocity structure of layer 3 suggests a restricted possible amount of hydrothermal alteration. Several observations favour the role of elevated temperatures for the presence of the anomalous velocity structure beneath the median valley. The seafloor bulge in the segment center and the continuous seamount chain off-axis suggest that the segment's melt supply is anomalously high. The high-temperature hydrothermal sites, situated on top of this bulge, indicate heat sources at shallow levels, and the abundance of fresh glassy sheet flows in the area denotes volcanic activity in recent years [*Haase et al.*, 2007]. Hence, the velocity reduction may result from a temperature anomaly due to a recent intrusion of melt.
Assuming that the observed velocity anomaly of 0.4-0.5 km/s is caused exclusively by elevated temperatures, this suggests that the axial portion of the mid crust is 700-900 K hotter than the ambient temperatures (for $dV/dT = -0.57 \cdot 10^{-3}$ km $s^{-1}$ $K^{-1}$ [*Christensen*, 1979]. Thermal models including hydrothermal circulation predict off-axis temperatures of 200-300 °C at depths of 2-2.5 km below seafloor [*Henstock et al.*, 1993] thus axial temperatures at the center of the northern segment may reach ~900-1200 °C at those depths. The solidus temperature of basalts, i.e. the onset of partial melting, depends on the MgO content in the form $T_s$(°C) = 18.3MgO (wt %) + 907 [*Sinton and Detrick*, 1992]. Possible MgO values can result in a wide range of solidus temperatures, but for a typical MgO MORB content of 9 wt% [*Schilling et al.*, 1983] would result in Ts ~1070 °C. Hence, the highest temperature likely reaches up to the solidus temperature. Since the tomographic method generally underestimates the amplitude of the anomaly (Fig. 11b), at least small portions of the mid crust on-axis may be partially molten.

### 6.2 Crustal structure and high-temperature hydrothermal venting

Our seismic models provide a detailed view into one type of geologic setting that can host high-temperature hydrothermal activity at the slow-spreading southern Mid-Atlantic Ridge. This setting seems to be different from ultramafic-hosted and tectonically controlled vent sites, which have been previously reported from the northern MAR e.g. at 36°15'N (Rainbow) and 26°10'N (TAG), and where for the latter seismic velocity models and earthquake hypocenters preclude the presence of a crustal melt reservoir [*deMartin et al.*, 2007; *Canales et al.,* 2007]. The segment north of the 5°S FZ is morphologically similar to the Lucky Strike segment near 37°N, where high-temperature hydrothermal venting occurs on top of a large seamount that forms the shallow center of a 65 km long ridge segment [*Langmuir et al.*, 1997]. A large axial magma chamber (AMC) is located at mid crustal depths (~3 km b.sf.) directly beneath the volcano, which led *Singh et al*. [2006] to suggest that this magma chamber provides the heat for the active hydrothermal vent above it and moreover, that magma chambers might be common features under long-lived hydrothermal fields at slow-spreading segments, particularly those within the rift valley, at or near the centre of segments, and hosted in basalt. At 23°20'N (MARK area), high-temperature vents are located over an elongated axial volcanic ridge (Snake Pit Ridge) and there is seismic evidence for mid-crustal magma in form of an axial LVZ [*Canales et al.,* 2000b] and some crustal MCS reflections, which appear to be linked to the roof of a transient magma chamber [*Calvert*, 1995].

At 5°S, the observation of thick crust beneath the central bulge may argue for a robust melt supply to the centre of the segment, where crust is formed by cooling and crystallization of magma in a crustal melt reservoir. The absence of MCS data, however, makes it impossible to discriminate between melt accumulated in thin lenses or more evenly distributed throughout the crust. Regarding the temperature structure, the existence of significant portions of melts is not required and the overall

morphology with a well-developed axial valley and the major bounding faults suggests that, apart from the central bulge, the crust is largely cool and brittle. *Haase et al.* [2007] concluded from measured fluid temperatures and composition at 5°S that the fluid's reaction zone at the Turtle Pits hydrothermal field is located very close (~150m) to the seafloor and that the vent field can be classified as "immediately post-eruptive", i.e. influenced by recent volcanic activity. The observed high-temperature hydrothermal vents might be linked to a recent diking and eruption event, reminiscent of the observed emplacement of lava flows at the East Pacific Rise, 9°50'N [*Soule et al.*, 2007]. If a corresponding diking event occurred at 5°S in 2002 related to the observed earthquake swarm (i.e. ~3 years before the fluid sampling but ~2 years after our seismic survey), our seismic velocity model would have sampled the pre-existing conditions.

### 6.3 Across-axis variations in crustal structure in the northern segment

The seismic model of Profile 11 reveals an average across-axis crustal thickness of 7.8±0.6 km for the northern segment center. A similar average crustal thickness of 7.5 km is found across the Reykjanes Ridge, a magmatically active axial volcanic ridge at the MAR at 59°N, where seismic, electromagnetic and magnetotelluric soundings provide convincing evidence for an axial magma chamber [*Sinha et al.*, 1998; *Navin et al.*, 1998]. But unlike 5°S, the crustal thickness at the Reykjanes Ridge is relatively constant; only minor thinning of 0.75 km is observed over a distance of 50 km off-axis. In the segment north of the 5°S FZ, there is no evidence for significant thinning by extensional faulting as the crust moves off-axis. Rather, progressing eastwards along Profile 11, the crust thickens from ~7.5 km on-axis to ~9 km over a distance of 10 km and then continuously thins eastwards to ~6 km at the line intersection of

Profiles 9 and 11 (Fig. 12c). Even if the increase in thickness might partly be an artefact of the short-scale morphology of the ridge flank, the trend to thicker crust east of the ridge-axis remains.

The average along-axis crustal thickness per segment (measured over a distance of 32 km from the segment center to the south) is 5.8±0.2 km for Profile 09 compared to 7.1±0.2 km for Profile 10. This suggests that the average melt supply per segment has increased in the northern segment by more than 20% within 3.3 Ma. This idea is confirmed by the observation that the continuous seamount chain in flow-line of the segment center shows gaps for distances greater than 60 km off-axis and finally seems to disappear at the edges of the bathymetric coverage (Fig. 1).

This irregular pattern may result from a temporal variability in the crustal emplacement process, which can either arise from a variable melt supply or asymmetries in the emplacement process. In the first scenario, the thicker crust beneath the ridge mountains was formed during a period of mantle melting in which the average melt production was higher than before and perhaps also higher than today. Based on observations of cyclic variations of the residual mantle Bouguer anomaly over the run of segments at 25°-27°N, *Tucholke et al.* [1997] suggest that episodic crustal thickening and thinning occurs at intervals of 2-3 Ma. They attribute this pattern to the periodic formation of buoyant melt diapirs and/or mantle heterogeneities [*Kuo and Forsyth*, 1988; *Lin et al.*, 1990]. Their results are compatible with seismic models, which reveal crustal thickness variations of 2-4 km across the ridge-axis within the predicted time scales [*Hosford et al.*, 2001; *Canales et al.*, 2000b]. However, in case of 5°S, the magmatic episode seems to persist at least over the last 3.7 Ma, reaching its maximum extent perhaps in the last 1 Ma.

In an alternative scenario, the differences in crustal thickness may simply arise from an asymmetric partitioning after the crust formed, with preferential thinning on the

western flank of the ridge axis. This asymmetry might be due to differences in the fault geometry of the flanks or to variations in crustal accretion; but it is rather unlikely that such a process can cause crustal thickness variations on the observed time-scale. Nevertheless, the lower topography west of the spreading axis suggests systematic asymmetries in the emplacement process or in the tectonic processes of rifting. However, the seismic model of Profile 11 cannot reveal such differences due to higher uncertainties for the western model portions (Fig. 10 center).

### 6.4 Along-axis variations in crustal structure in the northern segment

The seismic models of Profiles 9 and 10 suggest that the dominant style of crustal accretion in the northern segment has changed from a more two-dimensional to a strongly focused geometry. The observed change seems to coincide with a general increase in melt production of ~20%. About 4.1 Ma old crust of Profile 9 shows only minor thinning towards the transform and observed velocities indicate a rather uniform thickness of the lower crust. Hence, the northern segment portions of Profile 9 might fit into a MAR setting comprising e.g. the Kane FZ [*Abrams et al.,* 1988] and the Charlie Gibbs FZ [*Whitmarsh and Calvert,* 1986] which, as a perhaps common feature, lacks a pronounced crustal root in the segment center (Fig. 13e-f).
For ~0.8 Ma old crust (Profile 10), however, melt supply is strongly focused at the segment center, accompanied by a rapid reduction towards the transform, which might be one of the end-member styles of crustal accretion along slow-spreading ridges [*Kuo and Forsyth*, 1988; *Lin et al.*, 1990; *Tolstoy et al.*, 1993; *Detrick et al.*, 1995]. If seismic layer 3 represents the gabbroic portion of the crust, its reduction in thickness to 50% at the segment end and its almost complete absence beneath the transform suggests that the greatest volume of melt enters the crust at segment midpoints.

Seismic studies along the MAR near 35°N show a similar variation in crustal thickness from 8-9 km at the segment center to 2.5-5 km directly at the Oceanographer fracture zone (Fig. 13b-d) [*Hooft et al.,* 2000; *Canales et al.*, 2000a; *Sinha and Louden,* 1983; *Hosford et al.*, 2001; *Dunn et al.*, 2005]. Anomalously low velocity structures overlying the crustal root are interpreted as a magma plumbing system which redistributes the melts laterally and vertically through the overlying portions of the crust [*Magde et al.*, 2000]. Upon reaching the base of the lithosphere, the magma interacts with extensional tectonic stresses and propagates through the brittle layer both laterally and vertically as dikes. This mechanism is proposed to generate the observed relatively uniform thickness of the upper crust for the area near 35°N. A similar uniform structure for the upper crustal portion is consistently found in the segment north of the 5°S FZ. In this context, the observed low-velocity anomaly on Profile 11, which is centered at a depth of 2-3 km beneath the median valley, might correspond to a combination of increased temperatures and retained melt left behind by magmatic intrusions in a crustal plumbing system. In the view of *Magde et al.* [2000], this system would primarily extend in an along-axis direction due to extensional tectonic stresses and might be fed from a central source region probably located beneath the segment center bulge. At 5°S, however, the lack of a seismic profile along the axis of the rift valley precludes estimating the along-axis extent of this feature.

At the segment end, velocity depth functions of Profile 10 show significantly lower velocities compared to the segment midpoints (Fig. 12b). This is usually attributed to a dominant role of alteration and fracturing of the cooler and thinner crust and commonly observed in the proximity of fracture zones of slow and fast spreading ridges [*Detrick et al.*, 1993; *Canales et al.*, 2000a; *Van Avendonk et al.*, 1998]. These effects should have been much more subdued ~4.1 Ma ago due to the more uniform

along-axis temperature structure of the ridge at those time; in fact, a corresponding velocity decrease is barely visible on Profile 9 (Fig. 4, Fig. 12a).

### 6.5 Along-axis variations in crustal structure in the southern segment

The observed seismic velocity structure south of the transform fault suggests distinct along-axis lithological changes associated with an OCC at the 5°S ridge-transform intersection. As it is beyond the scope of this paper to discuss the detailed processes of OCC formation, only a brief discussion of the along-axis crustal structure is given here. Additional seismic refraction and gravity data, collected as part of the GERSHWIN experiment, will be presented elsewhere.

Beneath the areas of highest elevation and the transform facing flank of the OCC, a perhaps >10 km wide and up to 4 km thick model portion of high velocities (6-7 km/s) is placed at depths of <1 km beneath the seafloor. *Reston et al.* [2002] suggested on the basis of recovered lithologies obtained from three dredge hauls at the eastern scarp of the core complex that gabbro plutons intruded into serpentinized mantle rock might form a significant portion of the bulk lithology of the massif. Assuming the recovered lithologies are representative, the high-velocity body on Profile 9 might be interpreted as a large gabbro pluton or a mixed gabbroic/serpentine crust, provided the length scales of the matrix are too small to be resolvable in our tomographic models. There is seismic evidence for similar high-velocity bodies beneath three OCCs (Atlantis, Kane, and Dante OCC) where these structures are interpreted - based on extensive geological sampling and drilling results - as the gabbroic cores of the massifs [*Canales et al.*, 2008].

Close to 100 kilometers on Profile 9, the southern OCC termination curves southwards and forms a series of sub-basins which are the locus of a 2$^{nd}$ order ridge-

axis discontinuity (RAD) prior to the ridge-jump [*Reston et al.*, 2002]. Here, the thickness of the oceanic crust is reduced to ~2.5 km and seismic velocities increase almost linearly from 3.5 km/s at the seafloor to >7.0 km/s at the Moho. The presence of high velocity gradients and the absence of a normal layer 3 may be interpreted as a thin basaltic crust overlaying partially serpentinized mantle rock [e.g. *Detrick et al.,* 1993]. Velocities of 6-7 km/s on Profile 9 would indicate that 30-60% serpentinization will be required to reduce the compressional wave velocity of peridotite to these values [*Carlson and Miller*, 2003]. Upper mantle velocities <7.8 km/s at ~4.5 km depth would indicate a significant degree of serpentinization at least to those depths. Farther to the south, there is weak morphological evidence for renewed volcanism, and *Reston et al.* [2002] suggested that these areas might represent the continuation of the ridge-axis prior to the ridge jump. In the corresponding model portions of Profile 9, though sometimes beyond the areas of station coverage, velocities in the upper parts are low (6 km/s are not reached until ~2.0 km beneath the seafloor) and crustal thickness inceases again to ~4.5 km, which might argue for a magmatic crust south of the Moho bulge.

For the southern segment, our results indicate that melt extraction from the mantle formed a gabbro body beneath an oceanic detachment fault. This is consistent with recent studies which show that melt flux can be irregularly distributed within spreading segments [*Canales et al.*, 2008; *Dick et al.*, 2008]. Our tomographic model for Profile 9 suggests an increased melt flux beneath the transform facing flank of the OCC; the area of lowest melt supply is located close to the southern flank of the OCC next to a series of sub-basins which acted as a 2$^{nd}$ order RAD prior to the ridge-jump [*Reston et al.*, 2002].

### 6.6 Velocity structure of the transform valley

Because of the pronounced topography and the abrupt transition between completely different geological settings, the transform valley is a quite challenging place for the applied tomographic approach due to the lateral smoothing constraints employed. In case of Profile 10, a lower ray coverage in the uppermost model portions is related to an instrument failure at the transform floor and makes the interpretation of the resolved velocity structures somewhat more suspect. However, obtained velocity structures of both profiles differ fundamentally in the deeper resolved model portions. There is evidence for a well developed layer 3 as well as not much crustal thinning for Profile 9 compared to an either very thin or absent layer 3 and a crustal thickness reduced to perhaps less than 3 km for Profile 10 (Fig. 12a-b). For the latter, obtained velocity profiles also differ from corresponding velocity structures observed e.g. a few kilometers farther north at the segment end (Fig. 12b). Beneath the transform floor, obtained velocities are 0.4-0.8 km/s higher and velocity gradients are in the range of 1-2 $s^{-1}$ throughout the entire crustal section. In case of Profile 10, a mixed gabbroic/serpentine lower crust [e.g. *Cannat,* 1995] could be compatible with the present data provided the length scales of the matrix were small enough. Upper mantle velocities of 7.2-7.3 km/s would imply 20-25% serpentinization of mantle peridotite [*Carlson and Miller*, 2003]. Such a high percentage of serpentinization can only arise if the overlying rocks are highly fractured to provide pathways for seawater into the upper mantle, which has to be cooler than the 400-500°C limit for serpentinization [*Hacker et al.*, 2003].

Crustal thinning within the fracture zones to 2-3 km, in cases <1 km, and related to a very thin or absent seismic layer 3, seems to be a common observation at the MAR [e.g. *Purdy and Detrick*, 1986; *Sinha and Louden*, 1983; *Whitmarsh and Calvert*,

1986; *Louden et al.*, 1986; *White et al.*, 1992; *Detrick et al.*, 1993; *Hooft et al.*, 2000; *Canales et al.*, 2000a] and our tomographic results for Profile 10 support the prevailing view of diversion of magma from the segment ends. Along Profile 9, however, the observation of significant melt supply to the segment boundary demonstrates a possible exception from this rule.

## 7. Conclusions

The analysis of swath bathymetry and three seismic refraction profiles acquired at the Mid-Atlantic Ridge at 5° South suggests the following:

(1) The spreading segment north of the 5°S fracture zone is characterized by a well developed median valley with a pronounced seafloor bulge in the segment center and an associated seamount chain in flow-line of the segment center. It is thus of markedly contrasting character compared to the adjacent segment south of the FZ, where larger volcanic edifices are missing and spreading rather seems to be tectonically controlled.

(2) In the northern segment, crust with an age of ~0.8 Ma forms a pronounced root of 8.5 km in the segment center and thins rapidly along-axis to 2.8-3.5 km beneath the transform fault. The reduction in crustal thickness is almost exclusively accommodated by the thinning of velocity portions indicative of seismic layer 3. At the segment ends, lower velocities in the upper crustal portions may result from fracturing, facilitated by the greater tectonic deformation. Directly beneath the transform, high velocity gradients throughout the entire crustal section imply an either thin or absent seismic layer 3. These observations suggest that at those time melt flux from the mantle was strongly focused to the segment center.

(3) ~4.1 Ma old crust in the northern segment shows only minor thinning towards the segment end and observed velocities indicate a rather uniform thickness of the lower

crust. A well developed layer 3 can be traced up to the transform which demonstrates a significant melt supply to the segment boundary at those time. Our results suggest that the dominant style of crustal accretion in the northern segment has changed from a more two-dimensional to a strongly focused geometry. The observed change seems to coincide with a general increase in melt production of ~20% along this segment.

(4) Beneath the seafloor bulge in the northern segment center, anomalously low seismic velocities (-0.4 km/s compared to "background" velocities) at depths of 2.5 km b. sf. may indicate the presence of elevated temperatures and perhaps small portions of partial melt. These melts apparently provide the heat source for the high-temperature hydrothermal field which is situated directly above the velocity anomaly. Our results suggest that this segment is currently in a magmatically active period, which is confirmed by the abundance of fresh lavas at the seafloor.

(5) Across-axis in flow-line of the northern segment center, the crustal thickness varies between ~9 km and ~6 km around average values of 7.8 km. The observed variations suggest temporal changes in melt supply, although asymmetric tectonic processes of rifting, as indicated by the lower relief west of the ridge-axis, cannot be ruled out. The results are consistent with the observed along-axis variations in crustal structure which indicate a change in the amount and geometry of melt flux with time.

(6) South of the 5°S transform, the crust along our profile is thinnest (~2.5 km) beneath a series of sub-basins which acted as a 2$^{nd}$ order RAD prior to the ridge-jump. This area is characterized by an almost linear increase of crustal velocities with depth and upper mantle velocities <7.8 km/s. Towards the transform, the crustal thickness increases to ~5 km. A high-velocity body, which forms the crust beneath the transform facing flank of the OCC is interpreted as a large gabbro pluton or mixed gabbroic/serpentine matrix. The along-axis distribution of the apparent gabbro body at the OCC at 5°S suggests a significant melt flux at/near the transform and thus argues

for a more heterogeneous magma distribution than predicted by the prevailing view of diversion of magma from the segment ends.

**Acknowledgements**

We thank W. Weinrebe for the processing of the bathymetry data. The GMT software package [*Wessel and Smith*, 1995] was used in the preparation of this paper. RV METEOR cruise M47-2 and subsequent data analysis was funded by the Deutsche Forschungsgemeinschaft. Constructive reviews by J. P. Canales and A. Harding were much appreciated.

**References**

Abrams, L. J., R. S. Detrick, and P. J. Fox (1988), Morphology and crustal structure of the Kane Fracture Zone transverse ridge, *J. Geophys. Res.*, *93*, 3195–3210.

Berryhill, J. R. (1979), Wave-equation datuming, *Geophysics, 44*, 1329–1344.

Bickel, S.H. (1990), Velocity-depth ambiguity of reflection traveltimes, *Geophysics, 55,* 266-276.

Blackman, D. K., J.R Cann, B. Janssen and D.K. Smith (1998), Origin of extensional core complexes: Evidence from the Mid-Atlantic Ridge at Atlantis Fracture Zone, *J. Geophys. Res., 103,* 21,315–21,315.

Blackman, D. K., B. Ildefons, B.E. John, Y. Ohara, D.J. Miller, C.J. MacLeod, and Expedition 304/305 Scientists (2006), Proceedings of the Integrated Ocean Drilling Program, Volume 304/305: College Station, Texas, Integrated Ocean Drilling Program, doi: 10.2204/iodp.proc.304305.2006.

Calvert, A. J. (1995), Seismic evidence for a magma chamber beneath the slow-spreading Mid-Atlantic Ridge, *Nature, 377*, 410-414, doi:10.1038/377410a0.

Canales, J. P., R. S. D. J. Lin, and J. A. Collins (2000a), Crustal and upper mantle seismic structure beneath the rift mountains and across a non-transform offset at the Mid-Atlantic Ridge (35°N), *J. Geophys. Res*., *105*, 2699–2719.

Canales, J. P., J. A. Collins, J. Escartin, and R. S. Detrick (2000b), Seismic structure across the rift valley of the Mid-Atlantic Ridge at 23°20’ (MARK area): Implications for crustal accretion processes at slow spreading ridges, *J. Geophys. Res*., *105*, 28411-28425.

Canales, J. P., R. A. Sohn, and B. deMartin (2007), Crustal structure of the Trans-Atlantic Geotraverse (TAG) segment (Mid-Atlantic Ridge, 26°10’N): Implications for

the nature of hydrothermal circulation and detachment faulting at slow spreading ridges, *Geochem. Geophys. Geosyst.*, *8*, Q08004, doi:10.1029/2007GC001629.

Canales, J.P., B.E. Tucholke, M. Xu, J.A. Collins and D.L. DuBois (2008), Seismic evidence for large-scale compositional heterogeneity of oceanic core complexes, *Geochem. Geophys. Geosyst.*, *9*, Q08002, doi:10.1029/2008GC002009.

Cann, J. R., D.K. Blackman, D.K. Smith, E. McAllister, B. Janssen, S. Mello, E. Avgerinos, A. Pascoe, and J. Escartin (1997), Corrugated slip surfaces formed at North Atlantic ridge-transform intersections, *Nature, 385*, 329–332.

Cannat, M. (1995), Thin crust, ultramafic exposures, and rugged faulting patterns at the Mid-Atlantic Ridge (22°-24°N), *Geology*, *23*, 49-52.

Carlson, R. L., and D. J. Miller (2003), Mantle wedge water contents estimated from seismic velocities in partially serpentinized peridotites, *Geophys. Res. Letters*, *30*, 1250–1254.

Christensen, N. I. (1979), Compressional wave velocities in rocks at high in temperatures and pressures, critical thermal gradients and crustal low-velocity zones, *J. Geophys. Res.*, *84*, 6849–6857.

deMartin, B. J., R. A. Sohn, J. P. Canales, and S. E. Humphris (2007), Kinematics and geometry of active detachment faulting beneath the Trans-Atlantic Geotraverse (TAG) hydrothermal field on the Mid-Atlantic Ridge, *Geology*, *35*, 711-714.

DeMets, C., R. Gordon, D. F. Argus, and S. Stein (1990), Current plate motions, *Geophys. J. Int.*, *101*, 425–478.

Detrick, R. S., R. S. White, and G. M. Purdy (1993), Crustal structure of North Atlantic fracture zones, *Reviews of Geophysics*., *31*, 439–458.

Detrick, R. S., H. D. Needham, and V. Renard (1995), Gravity anomalies and crustal thickness variations along the Mid-Atlantic Ridge between 33°N and 40°N, *J. Geophys. Res.*, *100*, 3767–3787.

Dick, H. J. B., H.J. Natland, et al. (2000), A long in situ section of the lower oceanic crust: results of ODP leg 176 drilling at the Southwest Indian Ridge, *Earth Planet. Sci. Lett., 179*, 31–51.

Dick, H. J. B., M.A. Tivey, and B.E. Tucholke (2008), Plutonic foundation of a slow-spreading ridge segment: Oceanic core complex at Kane Megamullion, 23°30'N, 45°20'W, *Geochem. Geophys. Geosyst.*, *9*, Q05014, doi:10.1029/2007GC001645.

Dunn, R. A., V. Lekic, R. S. Detrick, and D. R. Toomey (2005), Three-dimensional seismic structure of the Mid-Atlantic Ridge 35°N: Evidence for focused melt supply and lower crustal dike injection, *J. Geophys. Res.*, *110*.

Escartin, J. and M. Cannat (1999), Ultramafic exposures and the gravity signature of the lithosphere near the Fifteen-Twenty Fracture Zones (Mid-Atlantic Ridge, 14°-16°N), *Earth Planet. Sci. Lett., 171*, 411–429.

Escartin, J., C. Mevel, C.J. MacLeod, and A.M. McCaig (2003), Constrains on deformation conditions and the origin of of oceanic detachments: the Mid-Atlantic Ridge core complex at 15°45'N, *Geochem. Geophys. Geosyst., 4,* 1067.

Flueh, E. R., and J. Bialas (1996), A digital, high data capacity ocean bottom recorder for seismic investigations, *Int. Underwater Systems Design*, *18*, 18–20.

Flueh, E. R., D. Klaeschen, and J. Bialas (2002), Options for multi-component seismic data acquisition in deep water, *First Break*, *20*, 764–769.

German, C. R., S. A. Bennet, D. P. Conelly, A. J. Evans, B. J. Murton, L. M. Parson, R. D. Prien, E. Ramirez-Llodra, M. Jakuba, T. M. Shank, D. R. Yoerger, E. T. Baker, S. L. Walker, and K. Nakamura (2008), Hydrothermal activity on the southern Mid-Atlantic Ridge: Tectonically- and volcanically-controlled venting at 4-5°S, *Earth Planet. Sci. Lett.*, *273*, 332-344.

Haase, K.M., S. Petersen, A. Koschinsky, R. Seifert, C. W. Devey, R. Keir, K. S. Lackschewitz, N. Dubilier, B. Melchert, M. Perner, O. Schmale, J. Süling, N. Dubilier, F. Zielinski, S. Fretzdorff, D. Garbe-Schönberg, U. Westernströer, C. R. German, T. M. Shank, D. Yoerger, O. Giere, J. Mawick, H. Marbler, C. Mertens, U. Stöber, M. Walter, C. Ostertag-Henning, H. Paulick, M. Peters, H. Strauss, S. Sander, J. Stecher, M. Warmuth, and S. Weber (2007), Young volcanism and related hydrothermal activity at 5°S on the slow-spreading southern Mid-Atlantic Ridge, *Geochem. Geophys. Geosyst.*, *8*, Q11002, doi:10.1029/2006GC001509.

Hacker, B. R., G. A. Abers, and S. M. Peacock (2003), Subduction factory I. theoretical mineralogy, densities, seismic wave speeds, and water contents, *J. Geophys. Res.*, *108*, 2029-2049.

Henstock, T. J., A. W. Woods, and R. S. White (1993), Accretion of oceanic crust by episodic sill intrusions, *J. Geophys. Res.*, *98*, 4143–4161.

Hobro, J. W. D., S. C. Singh, and T. A. Minshull (2003), Three-dimensional tomographic inversion of combined reflection and refraction traveltime data, *Geophys. J. Int.*, *152*, 79–93.

Hooft, E. E. E., R. S. Detrick, D. R. Toomey, J. A. Collins, and J. Lin (2000), Crustal thickness and structure along three contrasting spreading segments of the Mid-Atlantic Ridge 33.5-35°N, *J. Geophys. Res.*, *105*, 8, 205–226.

Hosford, A., J. Lin, and R. S. Detrick (2001), Crustal evolution over the last 2 m.y. at the Mid-Atlantic Ridge OH-1 segment, 35°N, *J. Geophys. Res.*, *106*, 13 269–13 286.

Karson, J. A. (1998), Internal structure of oceanic lithosphere: A perspective view from tectonic windows, in Buck, W. R., et others (Eds.), *Faulting and magmatism at mid-ocean ridges*, AGU, Geophysical monograph 106, pp. 177–218.

Kelemen, P.B., E. Kikawa, D.J Miller, and the Shipboard Scientific Party (2004), Proceedings of the Ocean Drilling Program, vol. 209, Ocean Drill. Program, College Station, Texas, doi: 10.2973/odp.proc.ir2209.2004.

Korenaga, J. (2000), TOMO2D - A C++ package for 2-D joint refraction and

reflection traveltime tomography, *http://earth.geology.yale.edu/~jk525/software/tomo2d.html*, pp. 1–11.

Korenaga, J., W. S. Holbrook, G. M. Kent, P. B. Kelemen, R. S. Detrick, H.-C. Larsen, J. R. Hopper, and T. Dahl-Jensen (2000), Crustal structure of the southeast Greenland margin from joint refraction and reflection seismic tomography, *J. Geophys. Res.*, *105*, 21 591–21 614.

Kuo, B. Y., and D. W. Forsyth (1988), Gravity anomalies of the ridge-transform system in the South Atlantic between 31 and 34.5°S: Upwelling centers and variations in crustal thickness, *Marine Geophysical Researches*, *10*, 205–232.

Langmuir, C., S. Humphris, D. Fornari, C. Van Dover, K. Von Damm, M. K. Tivey, D. Colodner, J.-L. Charlou, D. Desonie, C. Wilson, Y. Fouquet, G. Klinkhammer, and H. Bougault (1997), Hydrothermal vents near a mantle hot spot: the Lucky Strike vent field near 37°N on the Mid-Atlantic Ridge, *Earth Planet. Sci. Lett., 149*, 69-91.

Lin, J., and J. Phipps Morgan (1992), The spreading rate dependence of three-dimensional midocean ridge gravity structure, *Geophys. Res. Letters*, *19*, 13–16.

Lin, J., G. M. Purdy, H. Schouten, and J. C. Sempere (1990), Evidence from gravity data for focused magmatic accretion along the Mid-Atlantic Ridge, *Nature*, *344*, 627–632.

Louden, K. E., R. S. White, C. G. Potts, and D. W. Forsyth (1986), Structure and seismotectonics of the Vema Fracture Zone, Atlantic Ocean, *J. Geol. Soc. Lond.*, *143*, 795–805.

MacLeod, C. J., J. Escartin, D. Banerji, G. J. Banks, M. Gleeson, D. H. B. Irving, R. M. Lilly, A. M. McCaig, Y. Niu, and D. K. Smith (2002), Direct oceanic detachment faulting at the Mid-Atlantic Ridge, 15°45'N, *Geology*, *30*, 879-882.

Magde, L. S., and D.W. Sparks (1997), Three-dimensional mantle upwelling, melt generation and melt migration beneath segmented slow-spreading ridges, *J. Geophys. Res.*, *102* , B9 , 20571-20583.

Magde, L. S., A. H. Barcley, D. R. Toomey, R. S. Detrick, and J. A. Collins (2000), Crustal magma plumbing within a segment of the Mid-Atlantic Ridge, 35°N, *Earth Planet. Sci. Lett.*, *175*, 55–67.

Minshull, T. A. (1996), Along-axis variations in oceanic crustal density and their distribution to gravity anomalies at slow-spreading ridges, *Geophys. Res. Lett., 23*, 849-852.

Muller, M. R., T. A. Minshull, and R. S. White (1999), Segmentation and melt supply at the Southwest Indian Ridge, *Geology*, *27* , 867–870.

Muller, M. R., T. A. Minshull, and R. S. White (2000), Crustal structure of the Southwest Indian Ridge at the Atlantis II Fracture Zone, *J. Geophys. Res.*, *105*, 25 809–25 828.

Mutter, J. C., and J. A. Karsen (1992), Structural processes at slow-spreading ridges,

*Science*, *257*, 627-634.

Navin, D. A., C. Pierce, and M. C. Sinha (1998), The RAMESSES experiment-II. Evidence for accumulated melt beneath a slow spreading ridge from wide-angle refraction and multichannel reflection seismic profiles, *Geophys. J. Int.*, *135*, 746–772.

Purdy, G. M., and R. S. Detrick (1986), The crustal structure of the Mid-Atlantic Ridge at 23°N from seismic refraction studies, *J. Geophys. Res.*, *91*, 3139–3762.

Reston, T. J., W. Weinrebe, I. Grevemeyer, E. R. Flueh, N. C. Mitchell, L. Kirstein., C. Kopp, H. Kopp, and participants of METEOR 47/2 (2002), A rifted inside corner massif on the Mid-Atlantic Ridge at 5°S, *Earth Planet. Sci. Lett.*, *200*, 255–269.

Schilling, J. G., M. Zajac, R. Evans, T. Johnston, W. White, J. Devine, and R. Kingsley (1983), Petrologic and geochemical variations along the Mid-Atlantic Ridge from 27°N to 73°N, *American Journal of Science*, *283*, 510–586.

Shtivelman, V., and A. Canning (1988), Datum correction by wave-equation extrapolation. *Geophysics*, *53*, 1311–1322.

Singh, S. C., W. C. Crawford, H. Carton, T. Seher, V. Combier, M. Cannat, J. P. Canales, D. Düsünür, J. Escartin, and M. Miranda (2006), Discovery of a magma chamber and faults beneath a Mid-Atlantic Ridge hydrothermal field, *Nature*, *442*, 1029-1032, doi:10.1038/nature05105.

Sinha, M., and K. E. Louden (1983), The Oceanographer fracture zone: Crustal structure from seismic refraction studies, *Geophys. J. R. Astron. Soc.*, *75*, 713–736.

Sinha, M., S. C. Constable, C. Pierce, A. White, G. Heinson, L. M. MacGregor, D. A. Navin (1998), Magmatic processes at slow spreading ridges: implications of the RAMESSES experiment at 57°45'N on the Mid-Atlantic Ridge, *Geophys. J. Int.*, *135*, 731–745.

Sinton, J. M., and R. S. Detrick (1992), Mid-ocean ridge magma chambers, *J. Geophys. Res.*, *97*, 197–216.

Soule, S. A., D. J. Fornari, M. R. Perfit, and K. H. Rubin (2007), New insights into mid-ocean ridge volcanic processes from the 2005-2006 eruption of the East Pacific Rise, 9°46'N-9°56'N, *Geology*, *35*, 1079-1082, doi :10.1130/G23924A.1.

Spudich, P., and J. Orcutt (1980), A new look at the oceanic crust, *Rev. Geophys. Space Phys.*, *18*, 627–645.

Tilmann, F., E. R. Flueh, L. Planert, T. J. Reston, and W. Weinrebe (2004), Microearthquake seismicity of Mid-Atlantic Ridge at 5°S: A view of tectonic extension, *J. Geophys. Res.*, *109*, doi:10.1029/2003JB002,827.

Tolstoy, M., A. J. Harding, and J. A. Orcutt (1993), Crustal thickness on the Mid-Atlantic Ridge: Bull's eye gravity anomalies and characterized accretion, *Science*, *262*, 726–729.

Tucholke, B. E., and J. Lin (1994), A geological model for the structure of ridge segments in slow spreading ocean crust, *J. Geophys. Res., 99*, 11 937-11 958.

Tucholke, B. E., J. L. M. C. Kleinrock, and others (1997), Segmentation and crustal structure of the western Mid-Atlantic Ridge flank, 25°25'-27°10' N and 0-29m.y., *J. Geophys. Res.*, *102*, 10 203–10 223.

Tucholke, B. E., K. Fujioka, T. Ishihara, G. Hirt and M. Kinoshita (2001), Submersible study of an oceanic megamullion in the North Atlantic, *J. Geophys. Res., 106,* 16,145–16,162.

Van Avendonk, H. J. A., A. J. Harding, J. A. Orcutt, and W. S. Holbrook (1998), A two-dimensional tomographic study of the Clipperton transform fault, *J. Geophys. Res.*, *103*, 17 885-17 889.

Wessel, P., and W. H. F. Smith (1995), New version of the generic mapping tools released, *Eos Trans. AGU*, *76*, 329.

White, R. S., D. McKenzie, and R. K. O'Nions (1992), Oceanic Crustal Thickness From Seismic Measurements and Rare Earth Element Inversion, *J. Geophys. Res.*, *97*, 19 683–19 715.

Whitmarsh, R. B., and A. J. Calvert (1986), Crustal structure of Atlantic fracture zones, I, The Charlie Gibbs fracture zone, *Geophys. J. R. Astron. Soc.*, *85*, 107–138.

Wiener, N. (1949), *Extrapolation, interpolation, and smoothing of stationary time series*, New York, John Wiley and Sons, Inc.

Zelt, C.A. (1999), Modelling strategies and model assessment for wide-angle seismic traveltime data, *Geophys. J. Int., 139,* 183–204.

Zhang, J., and M. N. Toksöz (1998), Nonlinear refraction traveltime tomography, *Geophysics*, *63*, 1726–1737.

**Figure captions:**

Fig. 1: Bathymetric map of the Mid-Atlantic Ridge at 5° South based on Hydrosweep data collected during RV METEOR cruise M47-2. White circles and black lines mark the station distribution and shot geometry of the seismic refraction experiment. The 5°S transform fault divides the study area into two distinct spreading segments (thick white lines mark ridge-axis and transform). A high-temperature hydrothermal vent field (red triangle) is situated on top of the median valley seafloor bulge. Features discussed in text: ICH Inside corner high; HV halfmoon-like volcanoes; CV circular volcano.

Fig. 2: Record section of OBH71, Profile 11, with shot datums at seafloor (top) and sea level (center), respectively. (top): Downward continuation produced a good focussing and good restoration of the different seismic phases. The strong impact of the pronounced short-wavelength seafloor topography upon the seismic arrivals is markedly suppressed in the water-path corrected section. As a result, a strong PmP phase is visible. (center): Interpreted seismic arrivals are labeled: Pg (turning rays within the crust), PmP (reflected rays at the Moho), and Pn (turning rays in the upper

mantle). (bottom): Computed traveltimes (red dots) and associated pick uncertainties (blue bars). Corresponding ray paths through the final tomographic solution of Profile 11. Velocity contours are annotated in km/s. Only every third ray and traveltime is shown.

Fig. 3: Assessment of smoothing weights for velocity nodes (left) and depth nodes (right), testing different values in a single-step iteration. The optimal weight minimizes the roughness of the tomographic output and at the same time decreases significantly the data variance. Here shown for profile 09.

Fig. 4: (top): Final velocity model and Moho for Profile 09 derived from averaging all Monte Carlo solutions (RMS=54 ms). Grey shaded areas are 90% confidence intervals for Moho-depths from the uncertainty analysis. White Moho is directly controlled by reflection coverage. (center): Corresponding standard deviation for velocity and reflector nodes (dashed line, standard deviation is added to the corresponding reflector depth). Velocity contours are drawn at 0.05 km/s. (Bottom): Derivative weight sum for the final velocity model. All models are plotted with 5× vertical exaggeration. TF=transform fault; ICH=inside corner high.

Fig. 5: Point correlation shown for individual model parameters for Profile 09 (velocity nodes on the left and reflector nodes on the right). The black arrows indicate the position of the corresponding model parameter within the model space. A value close to (+1) or (−1) indicates correlation or anti-correlation with the corresponding model parameter. See text for discussion.

Fig. 6: (continued)

Fig. 6: Resolution test using different sets of synthetic velocity anomalies within the shallower crust (a) and within the lower crust/upper mantle (b). The background model is the smoothed tomographic output (velocities and reflector) of Fig. 4. As a starting model the "ensemble mean" mean model with the flat lying initial Moho is used (cf. figure A1). Recovery after 5 iterations is shown together with original output Moho (black line). (c): Synthetic velocity anomalies are placed beyond the instrument locations at mid-crustal depths. (d): Synthetic reflector (red line) constructed by adding a ±500 m perturbation with 40 km wavelength to the original reflector (black line).

Fig. 7: Model profile distributions and histograms for Moho depths for two selected profile intersections sampled from the 100 Monte Carlo ensembles of Profile 09. Corresponding values are shown for prior and posterior models, respectively. Top X-axis corresponds to velocity profiles (black lines), bottom X-axis corresponds to Moho depths (black histograms). (Left): Profile intersection taken on northern segment crust at 60 km. (Right): Profile intersection taken on inside corner crust of the southern segment at 102 km. Shaded backgrounds show, for reference purposes, the compilation of profiles in 1-7 Ma Atlantic crust of *White et al.* [1992]. Velocity is plotted as a function of depth below seafloor. Moho depths are binned at 0.1 km intervals.

Fig. 8: (top): Final velocity model and Moho for Profile 10 derived from averaging all Monte Carlo solutions (RMS=41 ms). Grey shaded areas are 90% confidence intervals for Moho-depths from the uncertainty analysis. White Moho is directly controlled by reflection coverage. The inset shows histograms for uppermost mantle

P-wave velocities for prior models (top) and posterior models (bottom). Velocity values are averaged between 93 km and 97 km profile distance and 1-1.5 km depth below the reflector for each model and are finally binned in 0.05 km/s intervals for all 100 Monte Carlo ensembles. Results reveal a cluster around average values of 7.2-7.3 km/s. (center): Corresponding standard deviation for velocity and reflector nodes (dashed line, standard deviation is added to the corresponding reflector depth). Velocity contours are drawn at 0.05 km/s. (Bottom): Derivative weight sum for the final velocity model. All models are plotted with 5× vertical exaggeration. TF=transform fault.

Fig. 9: (top): Point correlation calculated for a reflector node at 95 km profile distance. Results show almost no evidence for a remaining influence of the starting model. (bottom): Point correlation calculated for a velocity node placed at 95 km profile distance and 0.8 km depth beneath the Moho reflector. The black arrow indicates the position of the corresponding model parameter within the model space. Results suggest a stronger correlation with neighboring velocity nodes even across the Moho reflector. Hence, sub-Moho velocities may still suffer from interference with lower crustal velocities.

Fig. 10: (top): Final velocity model and Moho for Profile 11 derived from averaging all Monte Carlo solutions (RMS=57 ms). Grey shaded areas are 90% confidence intervals for Moho-depths from the uncertainty analysis. White Moho is directly controlled by reflection coverage. The inset shows the RMS data misfits for 400 Pn arrivals, recorded by three different stations, obtained by assuming different upper mantle velocities. For the forward calculations, the Monte Carlo derived velocities and reflector depths are used to define the crustal portion of the model. The smallest RMS values are obtained by assuming upper mantle velocities of 7.7-7.8 km/s. (center): Corresponding standard deviation for velocity and reflector nodes (dashed line, standard deviation is added to the corresponding reflector depth). Velocity contours are drawn at 0.05 km/s. (Bottom): Derivative weight sum for the final velocity model. All models are plotted with 5× vertical exaggeration. MV=median valley.

Fig. 11: (a) Reconstruction of a synthetic anomaly. The average velocity model of Profile 11 without the low velocity in the median valley is taken as the reference model for the synthetic anomaly (top). Inversion is started from the reference model. The recovered anomaly pattern after 15 iterations is shown at the bottom. (b): Observed velocity perturbation with depth at 48 km profile distance (black dashed line). The maximum perturbation is -0.4 km/s compared to "background" velocities (see text for details). The results of the synthetic test (red and solid black lines) are shown for comparison. (c): Point correlation calculated for a velocity node at 48 km profile distance in 2 km depth b. sf.

Fig. 12: Velocity depth profiles (averaged over 5 km profile distance) through northern segment crust, in comparison with an envelope of velocity depth profiles from the Mid-Atlantic Ridge for crust aged 0-7 Ma (*White et al.*, 1992). (a) Along-axis variations on Profile 09: at the segment center (extracted at 50 km profile distance; solid line), at the segment end (long-dashed line), and at the transform floor (short-dashed line). (b) Along-axis variations on Profile 10: at the segment center (solid line), at the segment end (long-dashed line), and at the transform floor (extracted at the deepest portion; short-dashed line). (c) Segment center crust on Profile 11: at 0 Ma (short-dashed line), at 0.8 Ma (Profile intersection with line 10;

long-dashed line), and 3 Ma (solid line). Black arrows indicate Moho depth; grey arrows show Moho depths for Atlantic crust aged <30 Ma from a compilation of *White et al.* [1992].

Fig. 13: Comparison of ridge-parallel profiles at various mid-ocean ridges (modified from *Muller et al.*, 2000). M= Moho; FZ= fracture zone; NTD= non-transform discontinuity; ICH=inside corner high. (a) Profile 10-MAR at 5°S (this study). (b)-(d) Mid-Atlantic Ridge (MAR) at the Oceanographer FZ (*Hooft et al.*, 2000; *Canales et al.*, 2000a; *Sinha and Louden,* 1983). (e) MAR at the Kane FZ (*Abrams et al.*, 1988). (f) MAR at the Charlie Gibbs FZ (*Whitmarsh and Calvert*, 1986). (g)-(h) Southwest Indian Ridge at 66°E (*Muller et al.*, 1999) and at Atlantis II FZ (*Muller et al.*, 2000). (i): Profile 09-MAR at 5°S (this study).

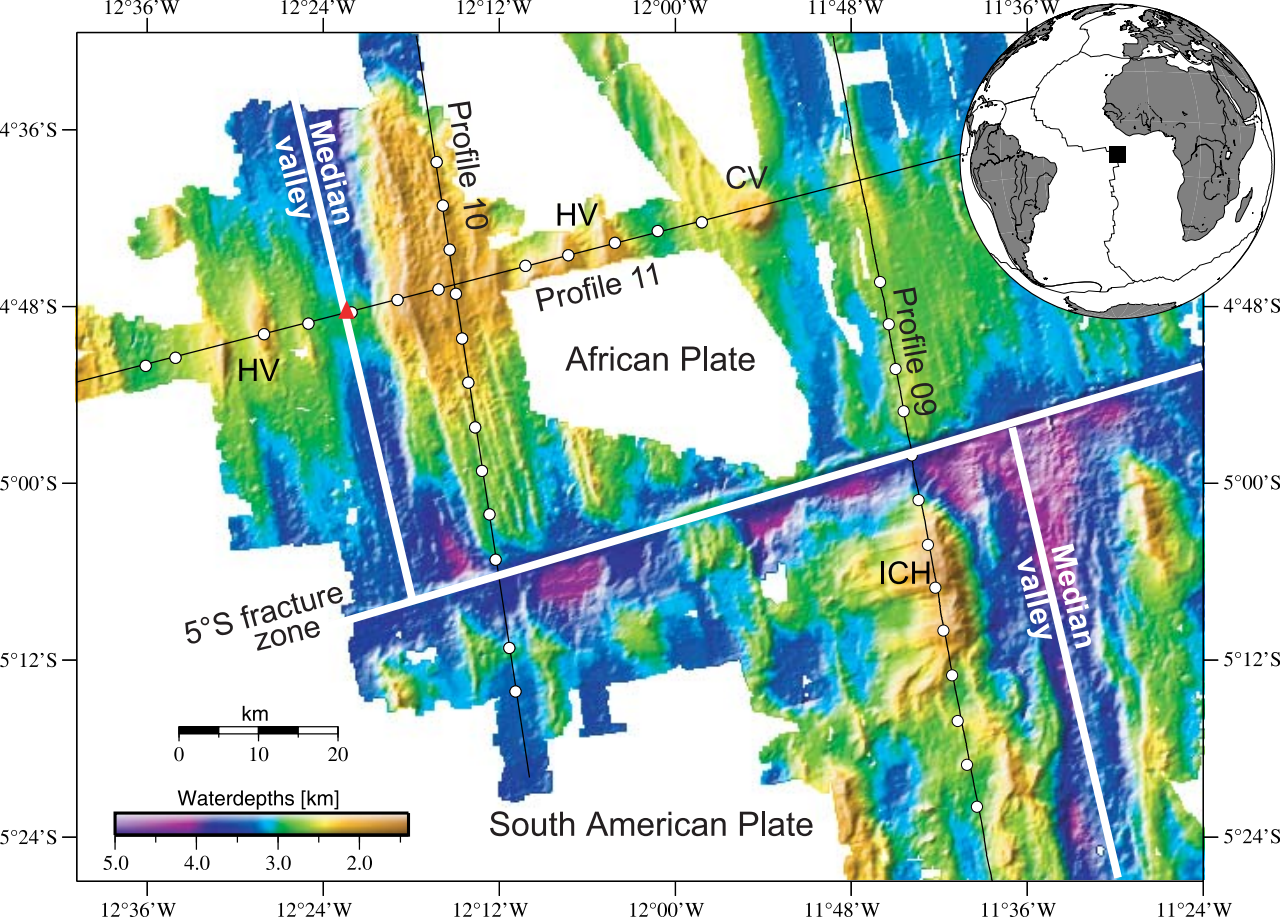
12°36'W
12°24'W
12°12'W
12°00'W
11°48'W
11°36'W
11°24'W
4°36'S
4°48'S
5°00'S
5°12'S
5°24'S
Median valley
Profile 10
Profile 11
Profile 09
HV
CV
African Plate
South American Plate
5°S fracture zone
ICH
km
0
10
20
Waterdepths [km]
5.0
4.0
3.0
2.0

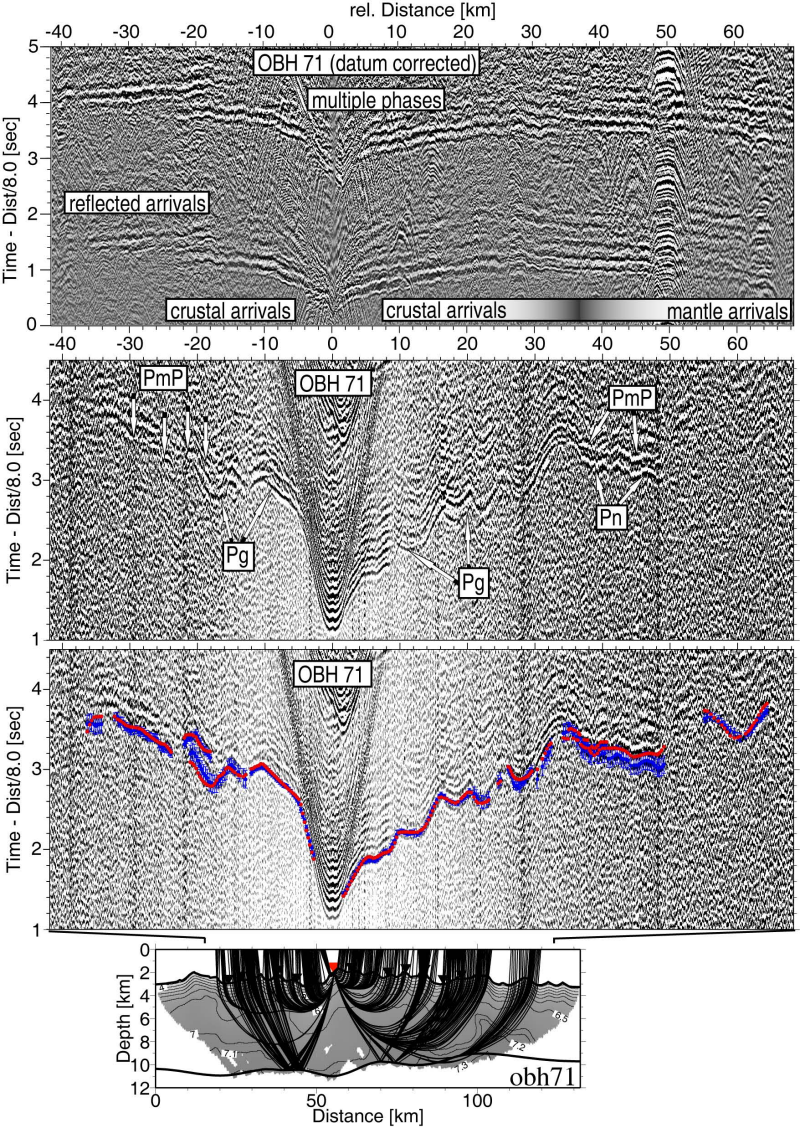
rel. Distance [km]
-40 -30 -20 -10 0 10 20 30 40 50 60
OBH 71 (datum corrected)
multiple phases
reflected arrivals
crustal arrivals
crustal arrivals
mantle arrivals
Time - Dist/8.0 [sec]
0 1 2 3 4 5
PmP
Pg
OBH 71
Pg
PmP
Pn
OBH 71
depth [km]
0 2 4 6 8 10 12
6.5
7
7.2
7.3
7.4
obh71
0 50 100
Distance [km]

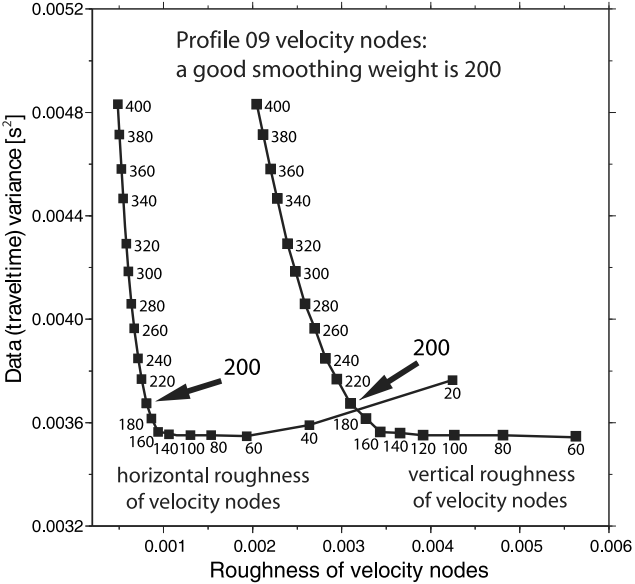
Profile 09 velocity nodes:
a good smoothing weight is 200
Data (traveltime) variance [s$^2$]
Roughness of velocity nodes
0.0052
0.0048
0.0044
0.0040
0.0036
0.0032
0.001
0.002
0.003
0.004
0.005
0.006
400
380
360
340
320
300
280
260
240
220
200
180
160
140
100
80
60
40
20
horizontal roughness
of velocity nodes
vertical roughness
of velocity nodes

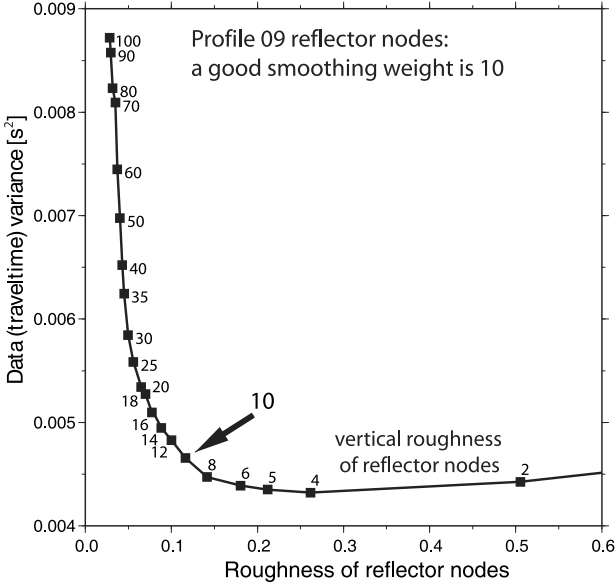
Profile 09 reflector nodes:
a good smoothing weight is 10
Data (traveltime) variance [s$^2$]
Roughness of reflector nodes
0.009
0.008
0.007
0.006
0.005
0.004
0.0
0.1
0.2
0.3
0.4
0.5
0.6
100
90
80
70
60
50
40
35
30
25
20
18
16
14
12
10
8
6
5
4
2
vertical roughness
of reflector nodes

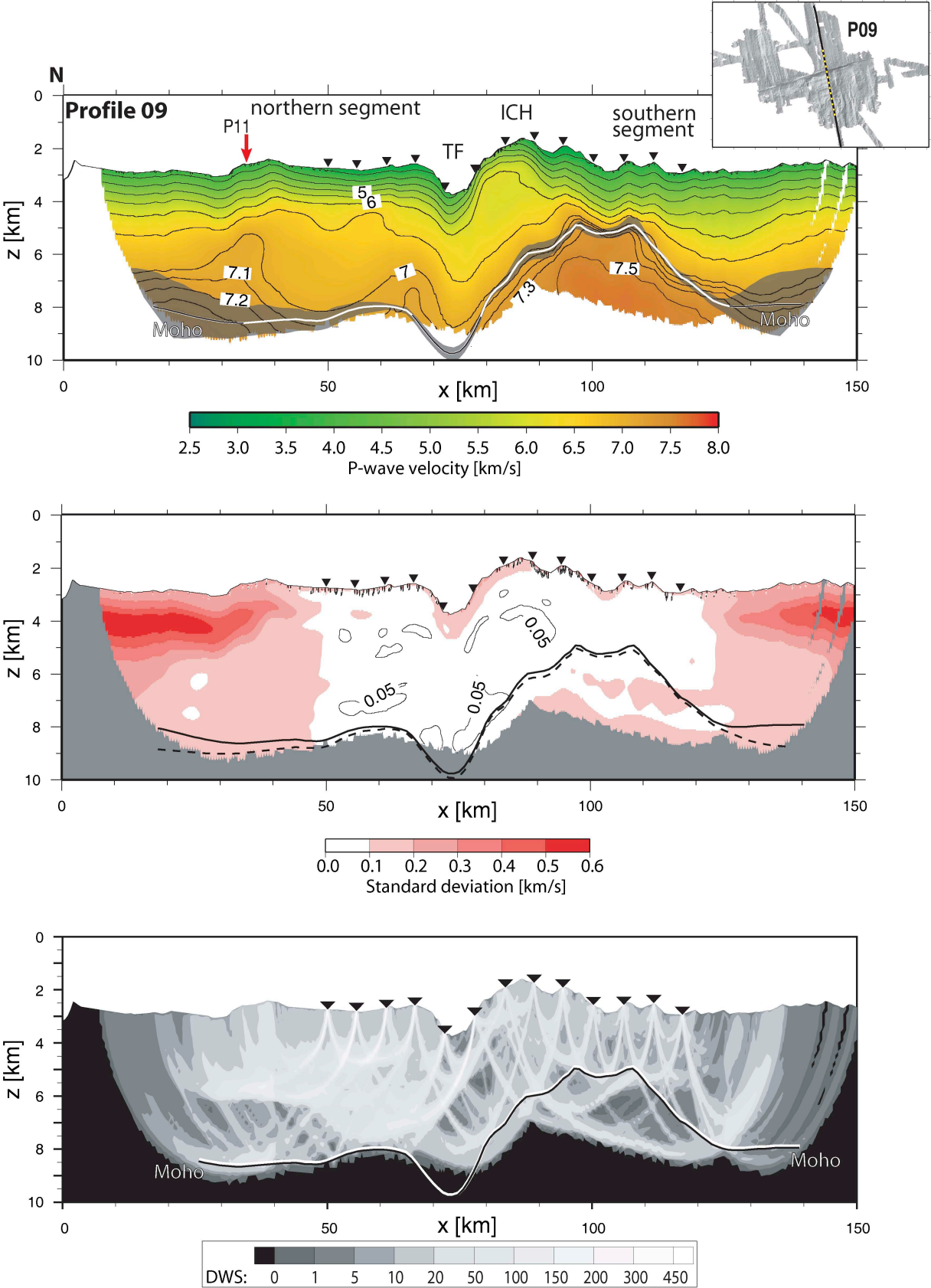
P09
N
Profile 09
northern segment
P11
TF
ICH
southern segment
5
6
7.1
7.2
7
7.3
7.5
Moho
Moho
z [km]
x [km]
2.5 3.0 3.5 4.0 4.5 5.0 5.5 6.0 6.5 7.0 7.5 8.0
P-wave velocity [km/s]
0.05
0.05
0.05
0.0 0.1 0.2 0.3 0.4 0.5 0.6
Standard deviation [km/s]
Moho
Moho
DWS: 0 1 5 10 20 50 100 150 200 300 450

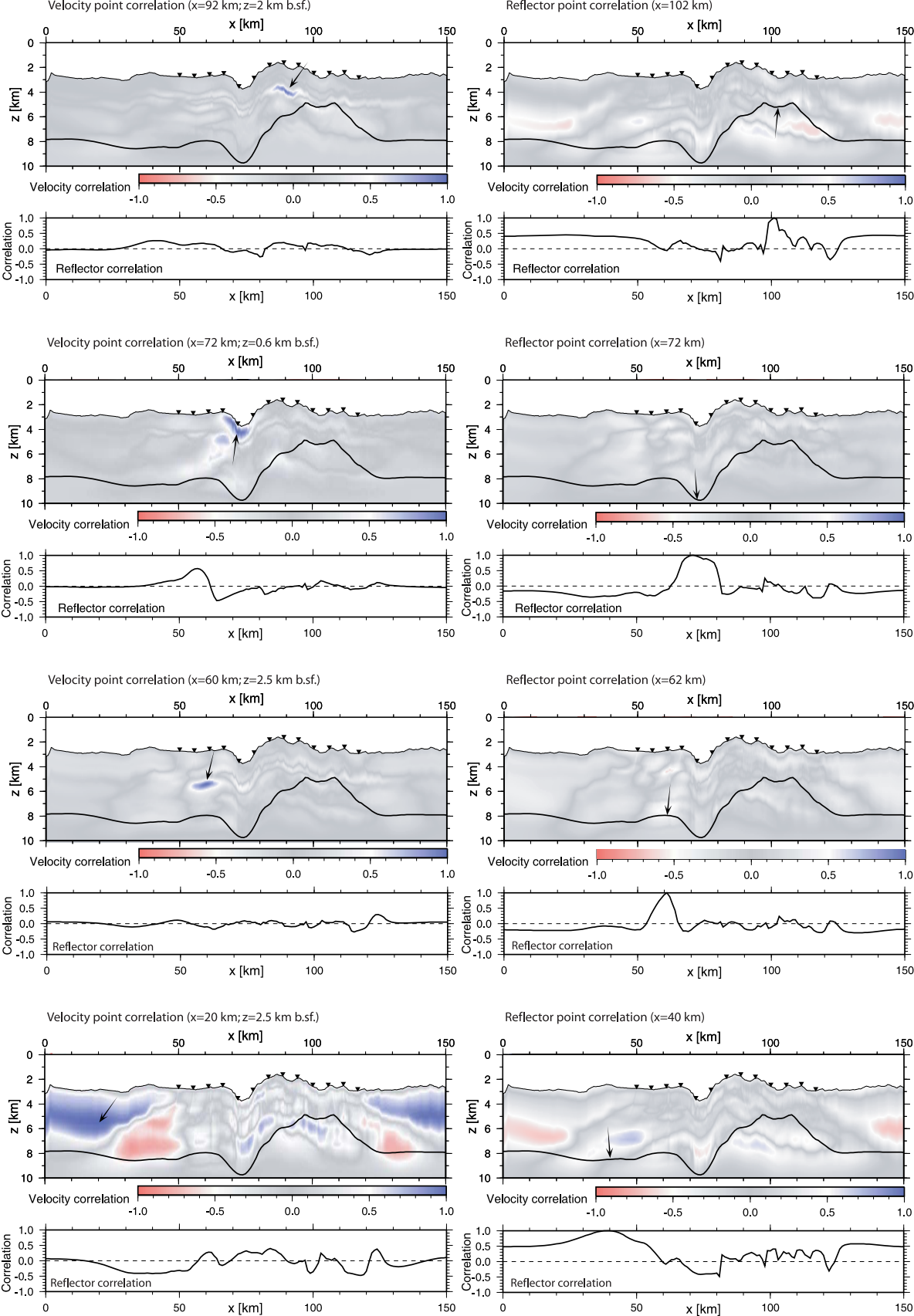
Velocity point correlation (x=92 km; z=2 km b.sf.)
Reflector point correlation (x=102 km)
Velocity point correlation (x=72 km; z=0.6 km b.sf.)
Reflector point correlation (x=72 km)
Velocity point correlation (x=60 km; z=2.5 km b.sf.)
Reflector point correlation (x=62 km)
Velocity point correlation (x=20 km; z=2.5 km b.sf.)
Reflector point correlation (x=40 km)
x [km]
z [km]
Velocity correlation
Correlation
Reflector correlation

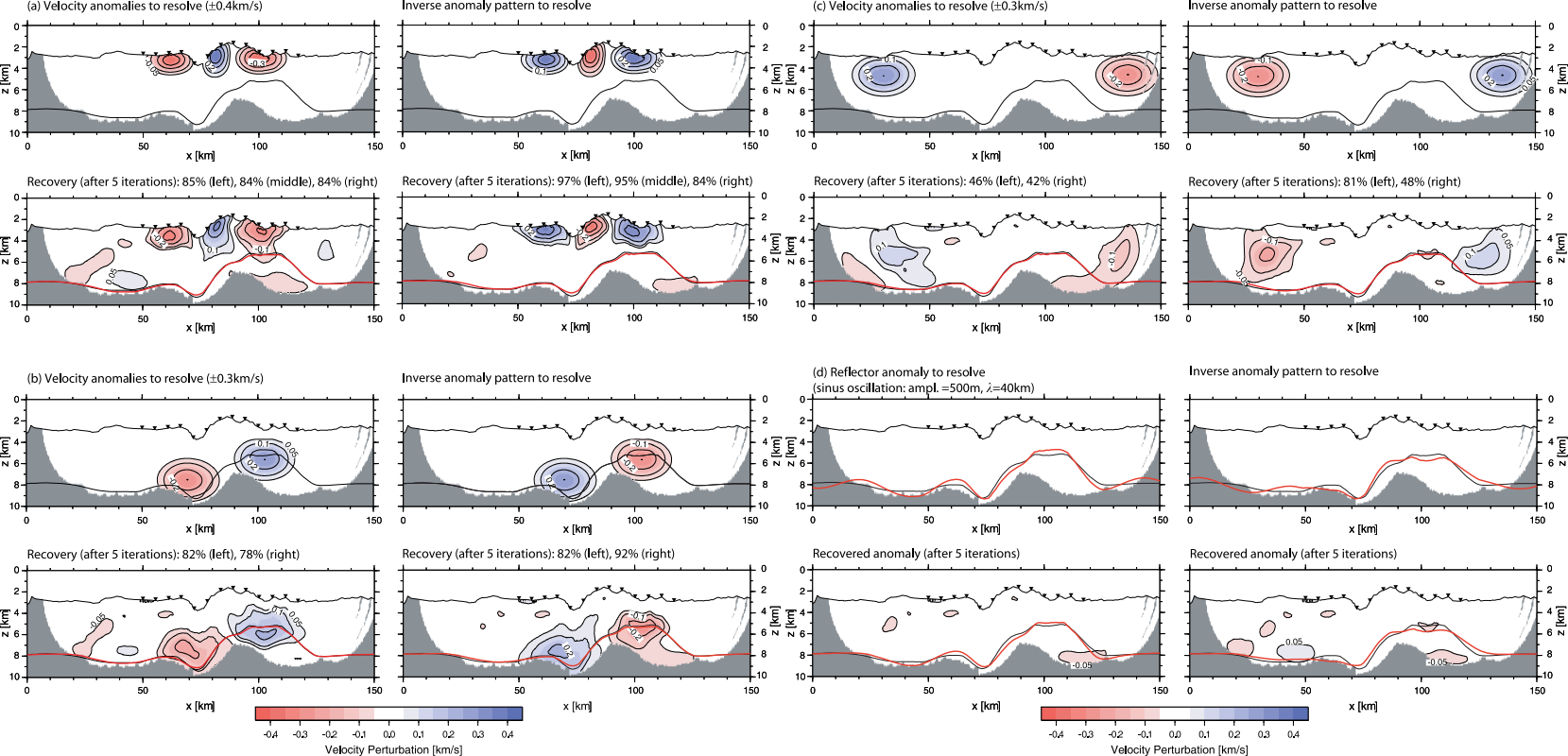
(a) Velocity anomalies to resolve (±0.4km/s)
Inverse anomaly pattern to resolve
(c) Velocity anomalies to resolve (±0.3km/s)
Inverse anomaly pattern to resolve
Recovery (after 5 iterations): 85% (left), 84% (middle), 84% (right)
Recovery (after 5 iterations): 97% (left), 95% (middle), 84% (right)
Recovery (after 5 iterations): 46% (left), 42% (right)
Recovery (after 5 iterations): 81% (left), 48% (right)
(b) Velocity anomalies to resolve (±0.3km/s)
Inverse anomaly pattern to resolve
(d) Reflector anomaly to resolve
(sinus oscillation: ampl. =500m, λ=40km)
Inverse anomaly pattern to resolve
Recovery (after 5 iterations): 82% (left), 78% (right)
Recovery (after 5 iterations): 82% (left), 92% (right)
Recovered anomaly (after 5 iterations)
Recovered anomaly (after 5 iterations)
z [km]
x [km]
Velocity Perturbation [km/s]
-0.4 -0.3 -0.2 -0.1 0.0 0.1 0.2 0.3 0.4

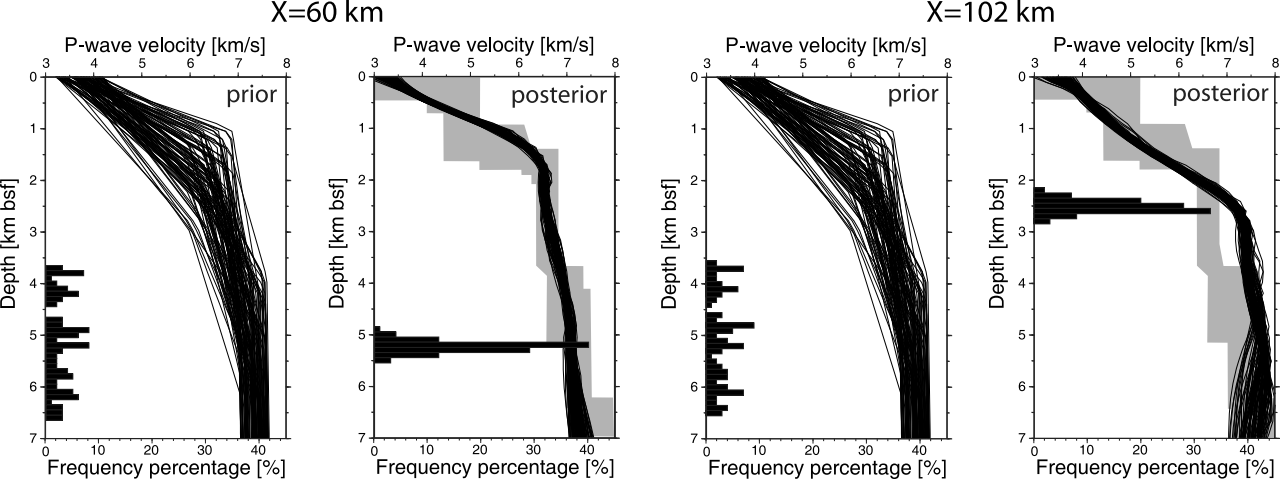
X=60 km
X=102 km
P-wave velocity [km/s]
prior
posterior
Depth [km bsf]
Frequency percentage [%]

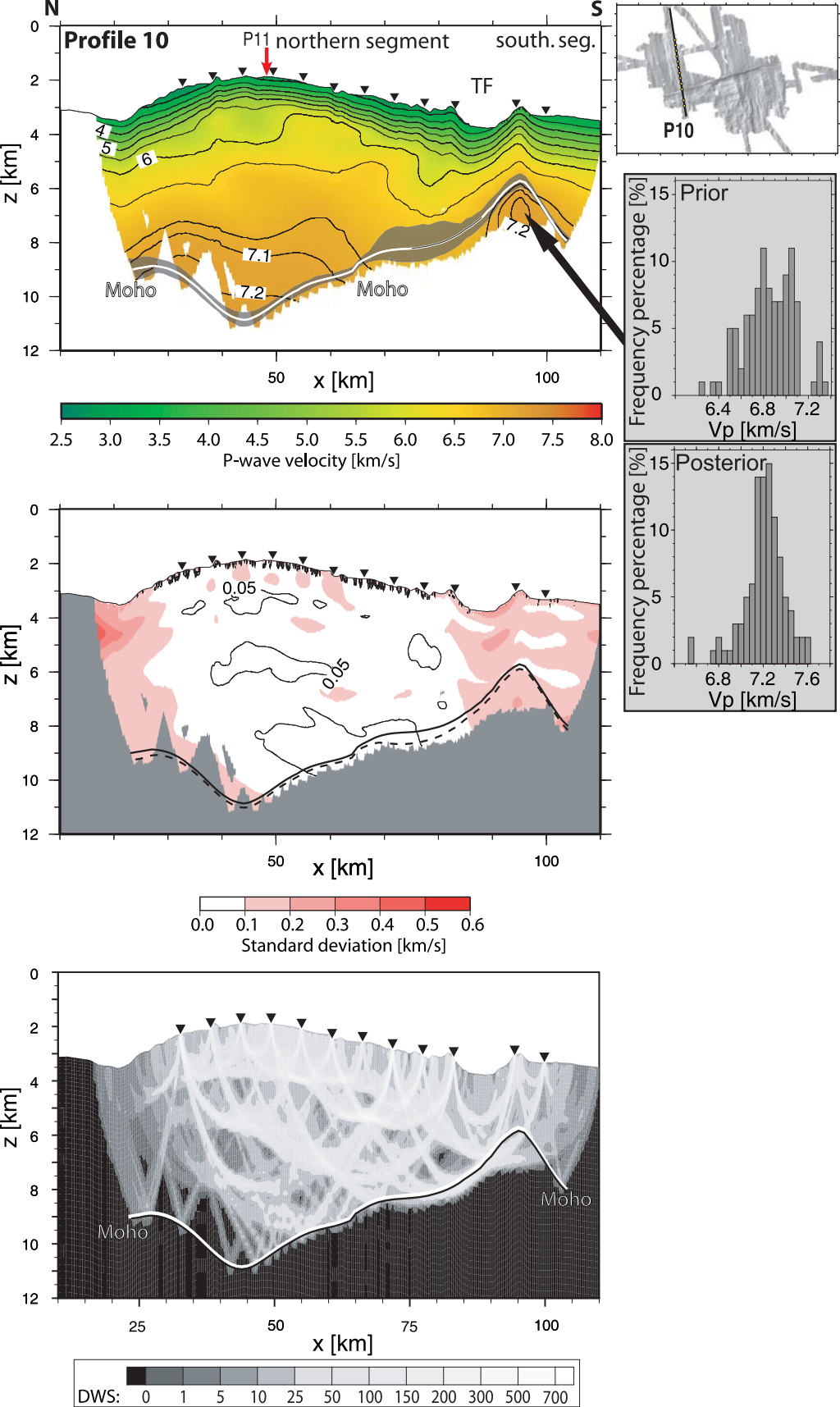
N
S
Profile 10
P11 northern segment
south. seg.
TF
4
5
6
7.1
7.2
Moho
Moho
z [km]
x [km]
P10
Prior
Frequency percentage [%]
Vp [km/s]
Posterior
2.5 3.0 3.5 4.0 4.5 5.0 5.5 6.0 6.5 7.0 7.5 8.0
P-wave velocity [km/s]
0.05
0.05
0.0 0.1 0.2 0.3 0.4 0.5 0.6
Standard deviation [km/s]
Moho
Moho
DWS: 0 1 5 10 25 50 100 150 200 300 500 700

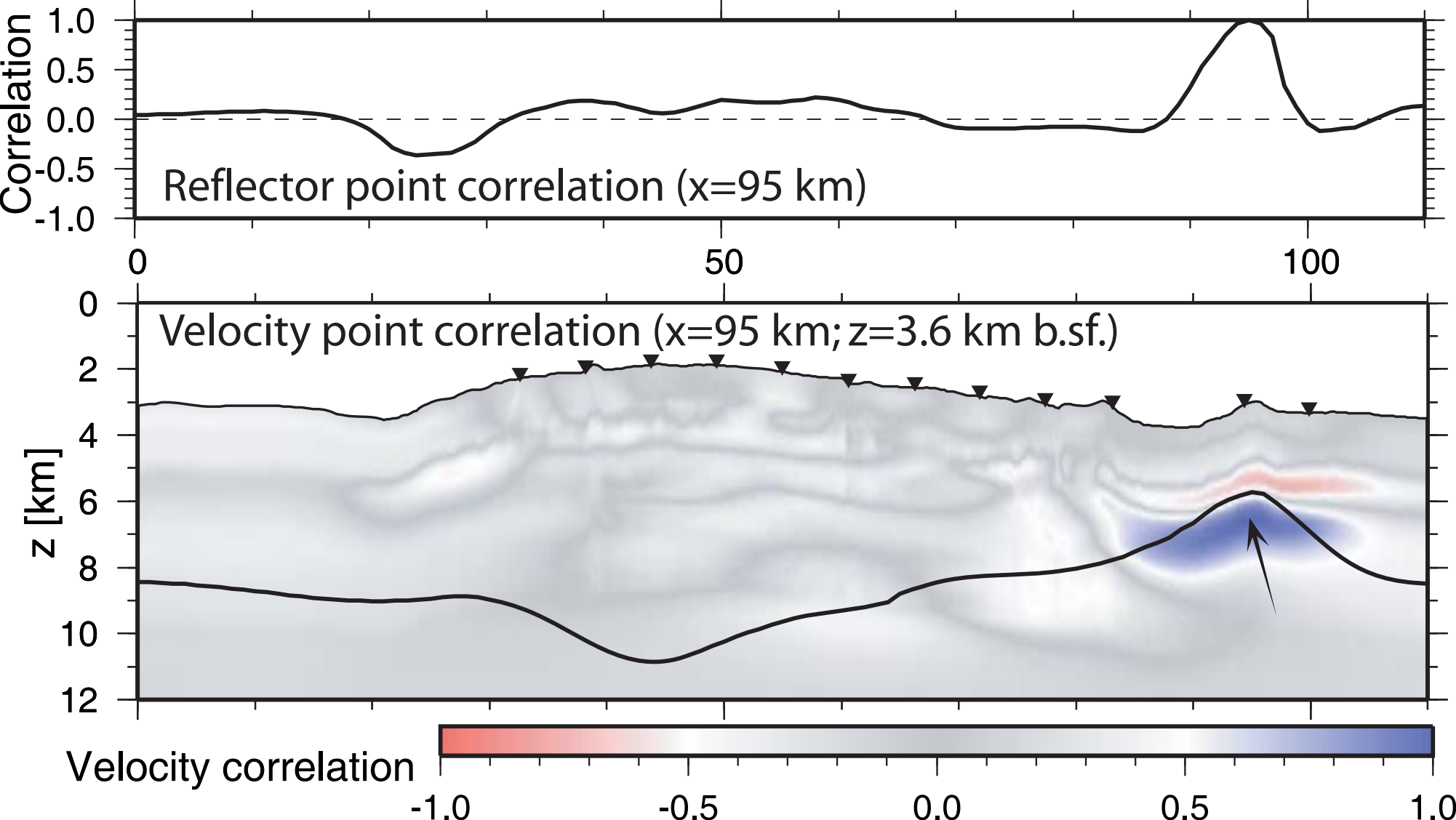
Correlation
1.0
0.5
0.0
-0.5
-1.0
Reflector point correlation (x=95 km)
0
50
100
Velocity point correlation (x=95 km; z=3.6 km b.sf.)
z [km]
0
2
4
6
8
10
12
Velocity correlation
-1.0
-0.5
0.0
0.5
1.0

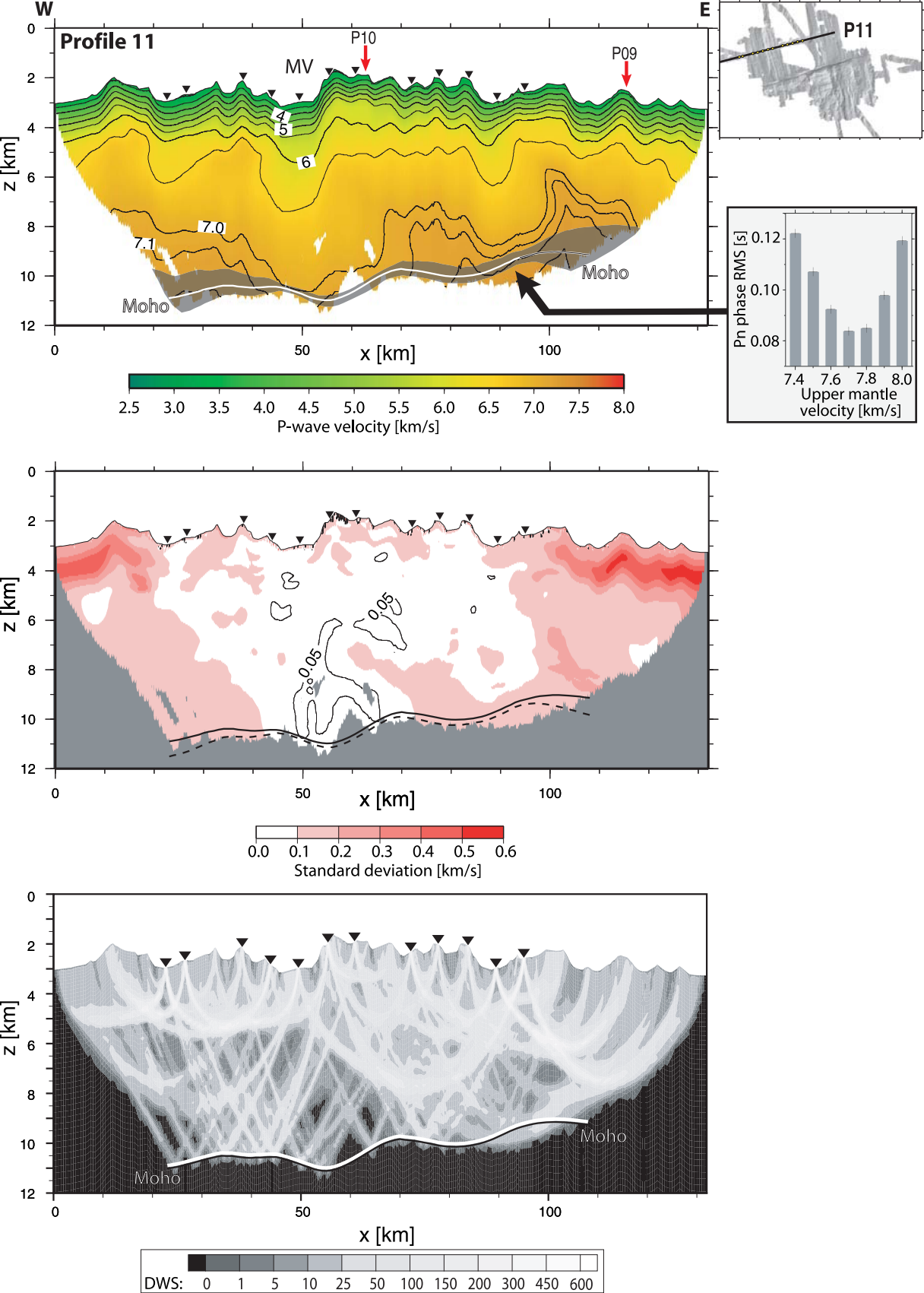
W
E
Profile 11
P10
MV
P09
P11
4
5
6
7.0
7.1
Moho
Moho
z [km]
x [km]
2.5 3.0 3.5 4.0 4.5 5.0 5.5 6.0 6.5 7.0 7.5 8.0
P-wave velocity [km/s]
Pn phase RMS [s]
0.12
0.10
0.08
7.4 7.6 7.8 8.0
Upper mantle velocity [km/s]
0.05
0.05
0.0 0.1 0.2 0.3 0.4 0.5 0.6
Standard deviation [km/s]
Moho
Moho
DWS: 0 1 5 10 25 50 100 150 200 300 450 600

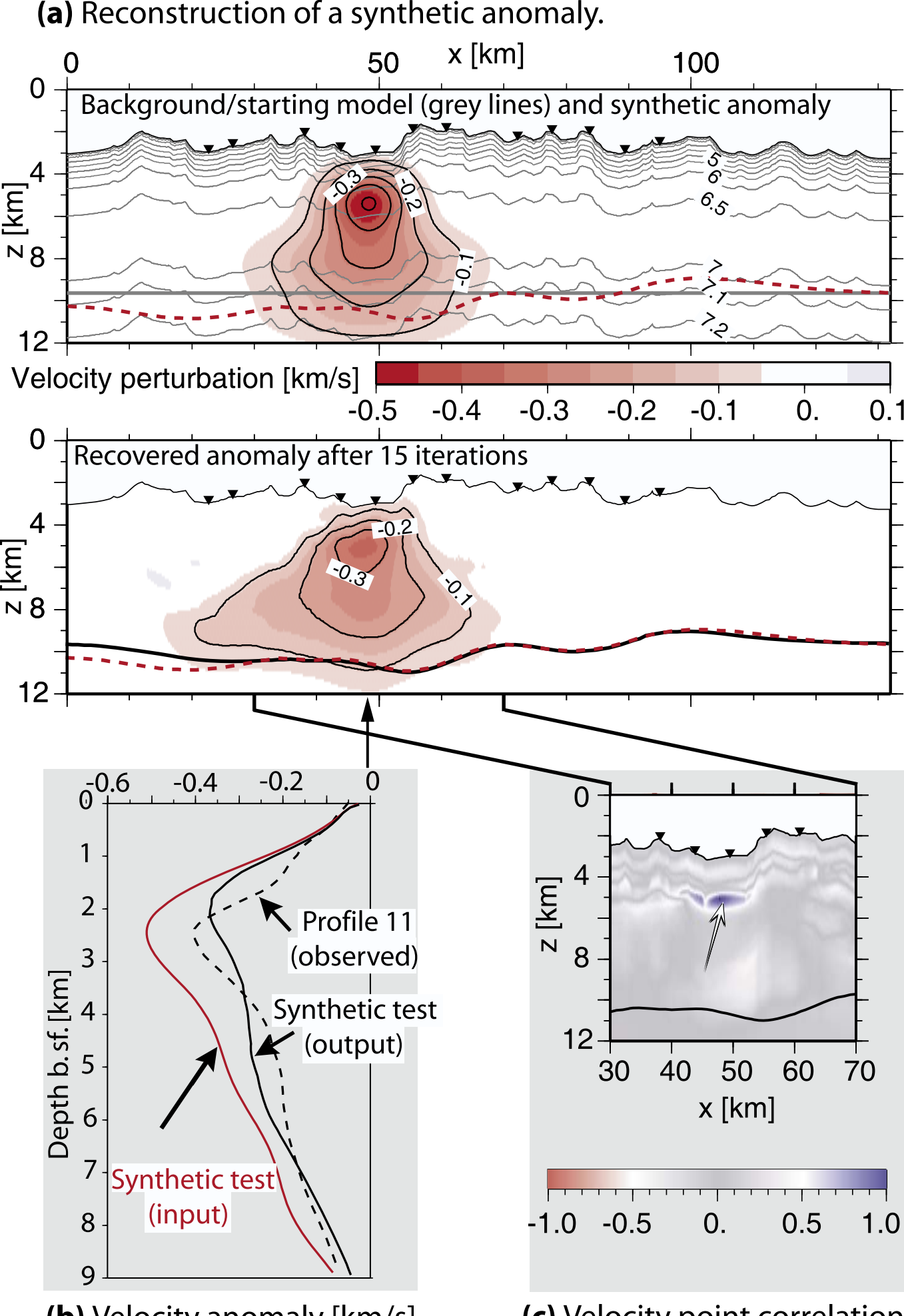
(a) Reconstruction of a synthetic anomaly.
x [km]
0
50
100
Background/starting model (grey lines) and synthetic anomaly
z [km]
-0.3
-0.2
-0.1
5.6
6.5
7
7.1
7.2
Velocity perturbation [km/s]
-0.5 -0.4 -0.3 -0.2 -0.1 0. 0.1
Recovered anomaly after 15 iterations
-0.6 -0.4 -0.2 0
Depth b.sf. [km]
Profile 11
(observed)
Synthetic test
(output)
Synthetic test
(input)
(b) Velocity anomaly [km/s]
30 40 50 60 70
x [km]
-1.0 -0.5 0. 0.5 1.0
(c) Velocity point correlation

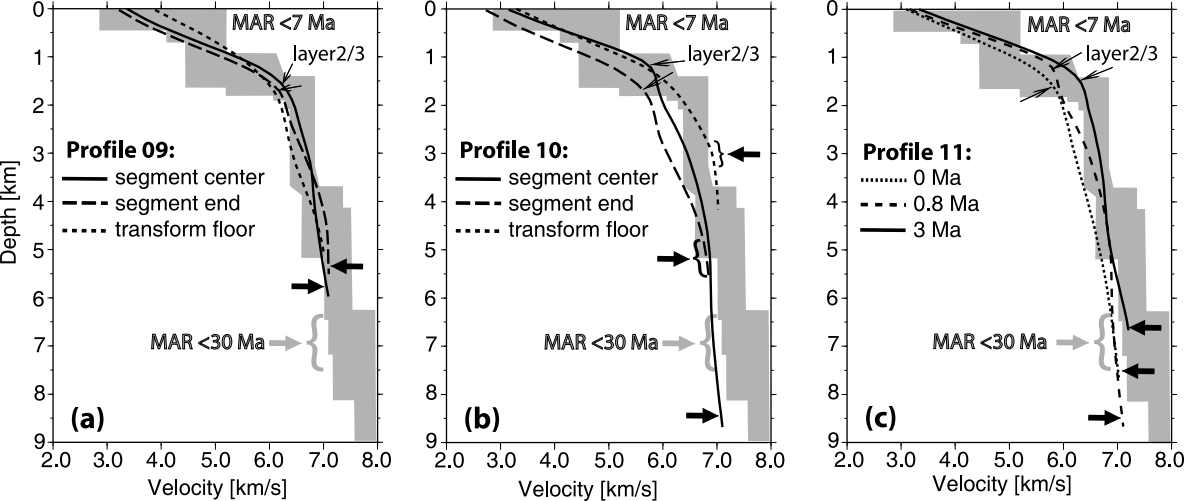
MAR <7 Ma
layer2/3
Profile 09:
segment center
segment end
transform floor
MAR <30 Ma
(a)
Profile 10:
segment center
segment end
transform floor
MAR <30 Ma
(b)
MAR <7 Ma
layer2/3
Profile 11:
0 Ma
0.8 Ma
3 Ma
MAR <30 Ma
(c)
Depth [km]
Velocity [km/s]
Velocity [km/s]
Velocity [km/s]

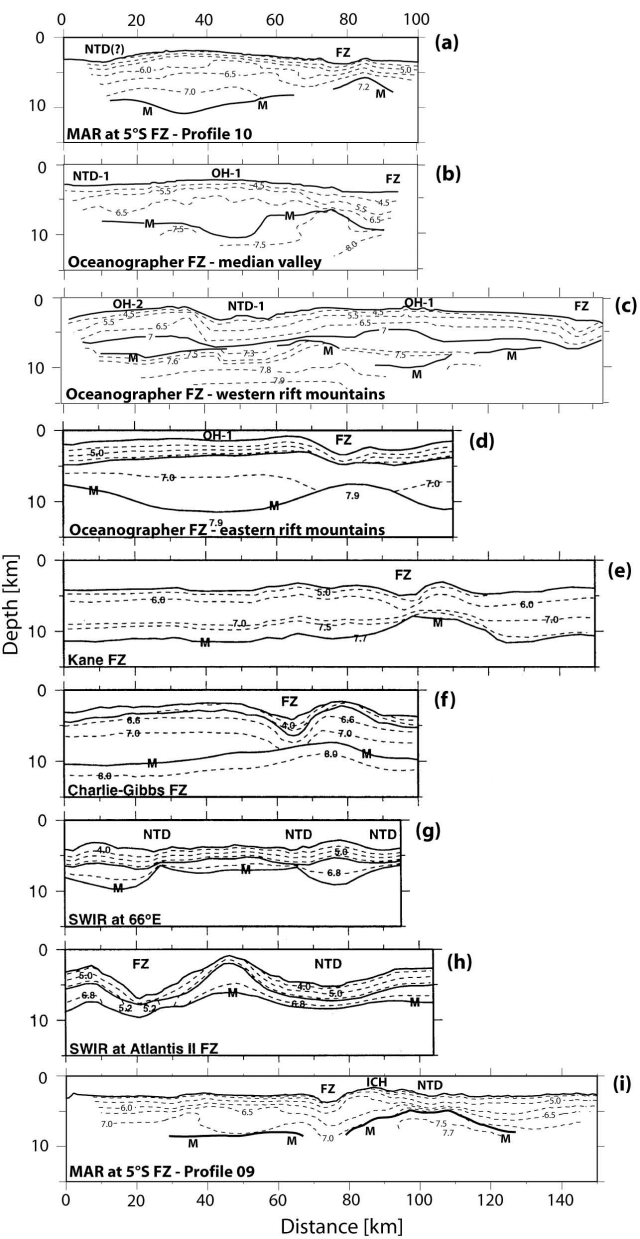
(a)
NTD(?)
FZ
MAR at 5°S FZ - Profile 10
(b)
NTD-1
OH-1
FZ
Oceanographer FZ - median valley
(c)
OH-2
NTD-1
OH-1
FZ
Oceanographer FZ - western rift mountains
(d)
OH-1
FZ
Oceanographer FZ - eastern rift mountains
(e)
FZ
Kane FZ
(f)
FZ
Charlie-Gibbs FZ
(g)
NTD
NTD
NTD
SWIR at 66°E
(h)
FZ
NTD
SWIR at Atlantis II FZ
(i)
FZ
ICH
NTD
MAR at 5°S FZ - Profile 09
Depth [km]
Distance [km]